

Non-Newtonian behavior and molecular structure of Coee bitumen under shear flow: a non-equilibrium molecular dynamics study

Claire A. Lemarchand,^{1, a)} Nicholas P. Bailey,² Billy D. Todd,³ Peter J. Daivis,⁴ and Jesper S. Hansen⁵

¹⁾*DNRF Centre “Glass and Time”, IMFUFA, Department of Sciences, Roskilde University, Postbox 260, DK-4000 Roskilde, Denmark*

²⁾*DNRF Centre “Glass and Time”, IMFUFA, Department of Sciences, Roskilde University, Postbox 260, DK-4000 Roskilde, Denmark*

³⁾*Department of Mathematics, Faculty of Science, Engineering and Technology, and Centre for Molecular Simulation, Swinburne University of Technology, Melbourne, Victoria 3122, Australia*

⁴⁾*School of Applied Sciences, RMIT University, Melbourne, Victoria 3001, Australia*

⁵⁾*DNRF Centre “Glass and Time”, IMFUFA, Department of Sciences, Roskilde University, Postbox 260, DK-4000 Roskilde, Denmark*

The rheology and molecular structure of a model bitumen (Cooee bitumen) under shear are investigated in the non-Newtonian regime using non-equilibrium molecular dynamics simulations. The shear viscosity, normal stress differences and pressure of the bitumen mixture are computed at different shear rates and different temperatures. The model bitumen is shown to be a shear-thinning fluid at all temperatures. In addition, the Cooee model is able to reproduce experimental results showing the formation of nanoaggregates composed of stacks of flat aromatic molecules in bitumen. These nanoaggregates are immersed in a solvent of saturated hydrocarbon molecules. At a fixed temperature, the shear-thinning behavior is related to the inter- and intramolecular alignment of the solvent molecules, but also to the decrease of the average size of the nanoaggregates at high shear rates. The variation of the viscosity with temperature at different shear rates is also related to the size and relative composition of the nanoaggregates. The slight anisotropy of the whole sample due to the nanoaggregates is considered and quantified. Finally, the position of bitumen mixtures in the broad literature of complex systems such as colloidal suspensions, polymer solutions and associating polymer networks is discussed.

^{a)}Electronic mail: clairel@ruc.dk

I. INTRODUCTION

Bitumen is one of the by-products of the refinery process of crude oil and a very viscous fluid. Its main application is as a binder in road pavement [1], because it combines many desirable properties: it is cheap, it adheres quite well to mineral filler particles and has suitable mechanical properties. Among bitumen's mechanical properties, the shear viscosity is of special importance. To guarantee a cohesive pavement, the shear viscosity should not be too low, while high values are often associated with a brittle behavior [2 and 3] which facilitates the development of cracks and eventually leads to the deterioration of the pavement. Bitumen's viscosity also has a great effect on the exploitation of bitumen reservoirs and transportation of bitumen. This is why the experimental literature reporting viscosity measurements of bitumen is so vast [1, 3–5]. Moreover, it is known that bitumen has a strong non-Newtonian behavior especially at low temperatures [6–9]. The non-Newtonian behavior is characterized by a strain rate dependent shear viscosity and is believed to originate from the specific molecular structure of bitumen [10], containing in particular asphaltene nanoaggregates [11].

Molecular dynamics (MD) is a good tool to study the molecular structure of bitumen and of the asphaltene nanoaggregates [12–15]. MD simulations can also quantify the mechanical properties of the material. Indeed, there are a few numerical studies relating the shear viscosity of bitumen in the limit of vanishing strain rate to its molecular and supramolecular structure [16–19]. However, to our knowledge, there has been no MD study relating the non-Newtonian behavior of bitumen to its molecular structure, in particular to the nanoaggregate structure. That is the first aim of this article. A second aim is to compare the molecular structure of bitumen under shear to that of other complex systems such as colloidal suspensions [20], polymer solutions [21], and associative polymer networks [22]. The hope is then to gain some insights on which structural characteristics of bitumen to focus on to model its rheology.

In order to achieve these aims, we used non-equilibrium molecular dynamics simulations with the SLLOD algorithm [23 and 24]. This algorithm is able to reproduce a shear Couette flow, even far from equilibrium [23] and provide the value of the

shear rate dependent viscosity. The SLLOD algorithm has been used to simulate shear flow of complex systems such as hyperbranched polymers [25], associating polymer solutions [26] and ionic liquids [27]. In this paper, we applied it to Cooe bitumen [28], which is a four-component bitumen model describing a bitumen with generic mechanical properties [17] and molecular structure [18 and 29]. Different temperatures were investigated in order to extrapolate the results to ambient temperature.

The paper is organised as follows. Section II contains information about the model bitumen used and the SLLOD algorithm. Results for the rheological properties and the molecular structure of the sample are presented and discussed in Secs. III and IV. Finally, Sec. V contains a summary and a discussion.

II. SIMULATION DETAILS

A. Cooe bitumen

The chemical composition of bitumen is very complex [30]. However, the molecules in bitumen can be classified into dissolution classes. The SARA classification [31] is one of the most common classifications and it distinguishes between Saturated hydrocarbons, resinous oil molecules, called Aromatic in the SARA scheme, Resin molecules and Asphaltene molecules. All of the last three molecule types are aromatic and the molecular weight of asphaltene molecules is on average higher than that of resin molecules, which is higher than the resinous oil molecular weight. To obtain a simple model of a generic bitumen, one typical molecular structure for each class was chosen. The molecular structures chosen are shown in Fig. 1. The reasons behind these specific choices are given in Ref. [17]. The main system studied in this paper contains in weight fraction: 57.1% of saturated hydrocarbons, 7.6% of resinous oil molecules, 13.8% of resin molecules, and 21.5% of asphaltene molecules. The total number of united atom units in the system is 15570. The methyl (CH_3), methylene (CH_2), and methine (CH) groups are represented by the same united atom unit of molar mass $13.3 \text{ g}\cdot\text{mol}^{-1}$ and the sulfur atoms are represented by a united atom unit with a different molar mass $32 \text{ g}\cdot\text{mol}^{-1}$. The

interaction potential between the united atom units contains four terms. The first term corresponds to an intermolecular potential. It is a Lennard-Jones potential of the form $U_{LJ}(r) = 4\epsilon((\sigma/r)^{12} - (\sigma/r)^6)$ with parameters $\sigma = 3.75 \text{ \AA}$ and $\epsilon/k_B = 75.4 \text{ K}$, where r is the interatomic distance and k_B the Boltzmann constant. The method of shifted potential is used with a cutoff of 2.5σ . The three other terms of the interaction potential describe intramolecular interactions. They control the bond length between two connected particles, the angle between three consecutive particles, and the dihedral angle between four consecutive particles. They are given by the following expression:

$$\begin{aligned}
 U_{\text{intra}}(\mathbf{r}) = & \frac{1}{2} \sum_{\text{bonds}} k_s (r_{ij} - l_b)^2 \\
 & + \frac{1}{2} \sum_{\text{angles}} k_\theta (\cos \theta - \cos \theta_0)^2 + \sum_{\text{dihedrals}} \sum_{n=0}^5 c_n \cos^n \phi.
 \end{aligned} \tag{1}$$

The values of the parameters k_s , l_b , k_θ , θ_0 , and c_n are listed in a previous work [17]. The simulations were performed at four different temperatures: 377 K, 452 K, 528 K, and 603 K and at constant density. For each temperature, the chosen density corresponds to an average equilibrium pressure equal to the atmospheric pressure. The four densities chosen are: $1007 \text{ kg}\cdot\text{m}^{-3}$, $964 \text{ kg}\cdot\text{m}^{-3}$, $894 \text{ kg}\cdot\text{m}^{-3}$, and $833 \text{ kg}\cdot\text{m}^{-3}$.

B. SLLOD algorithm

In this work, the molecular version of the SLLOD algorithm [23 and 25] is used to obtain a shear flow of the bitumen mixture. The equations of motion in that case are given by:

$$\dot{\mathbf{r}}_{i\alpha} = \frac{\mathbf{p}_{i\alpha}}{m_{i\alpha}} + \mathbf{r}_i \cdot \nabla \mathbf{u}, \tag{2}$$

$$\dot{\mathbf{p}}_{i\alpha} = \mathbf{F}_{i\alpha} - \frac{m_{i\alpha}}{M_i} \mathbf{p}_i \cdot \nabla \mathbf{u} - \zeta \frac{m_{i\alpha}}{M_i} \mathbf{p}_i, \tag{3}$$

where $\mathbf{r}_{i\alpha}$ and $\mathbf{p}_{i\alpha}$ are the laboratory position and peculiar momentum of particle α in molecule i , respectively (peculiar means that the corresponding velocities are relative to the streaming/flow velocity), $\mathbf{F}_{i\alpha}$ is the force acting on particle α in molecule i , $\nabla \mathbf{u}$ is the velocity gradient tensor, chosen here such that the (x, y)

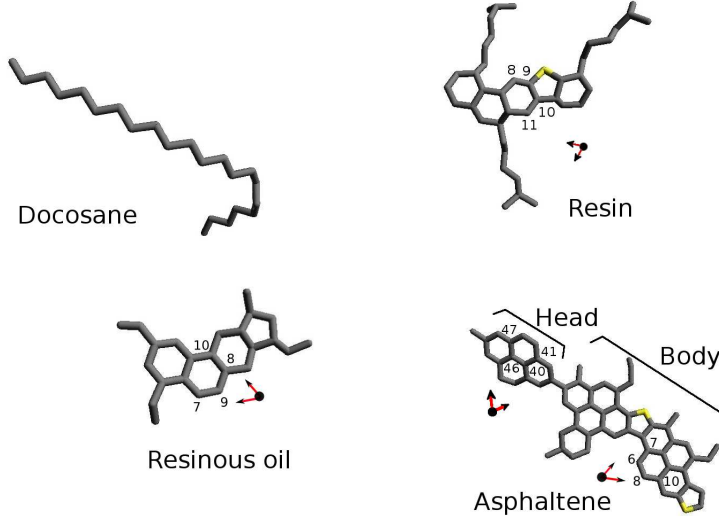


FIG. 1. (Color online) Structure of the four molecules in the "Cooee bitumen" model. Grey edges represent the carbon groups CH_3 , CH_2 and CH and yellow edges represent sulfur atoms. The "head" and "body" of the asphaltene molecule are shown. Numbers and arrows indicate bond-vectors used to quantify the nanoaggregate structure. Reproduced from Ref. [18], (Copyright 2013 AIP).

component is $\partial u_x / \partial y = \dot{\gamma}$ and all other components are zero, $\mathbf{r}_i = \sum_{\alpha=1}^{N_i} m_{i\alpha} \mathbf{r}_{i\alpha} / M_i$ is the position of the center of mass of molecule i , $M_i = \sum_{\alpha=1}^{N_i} m_{i\alpha}$ is the mass of molecule i , $\mathbf{p}_i = \sum_{\alpha=1}^{N_i} \mathbf{p}_{i\alpha}$ is the momentum of the center of mass of molecule i , N_i is the number of particles in molecule i , and ζ is the Gaussian thermostat multiplier given by:

$$\zeta = \frac{\sum_{i=1}^{N_m} \mathbf{F}_i \cdot \mathbf{p}_i / M_i - \dot{\gamma} \sum_{i=1}^{N_m} p_{ix} p_{iy} / M_i}{\sum_{i=1}^{N_m} \mathbf{p}_i^2 / M_i}, \quad (4)$$

where $\mathbf{F}_i = \sum_{\alpha=1}^{N_i} \mathbf{F}_{i\alpha}$ is the force acting on molecule i and N_m the total number of molecules. The expression for the thermostat multiplier ζ corresponds to the application of Gauss' principle of least constraint, used to keep the molecular center of mass kinetic temperature constant. The algorithm used to propagate the SLLOD equations of motion is the operator splitting algorithm developed by Pan *et al* [32] and adapted for molecular SLLOD equations of motion. To our knowledge, it is the first time that the operator splitting algorithm has been adapted to molecular systems. This implementation is described in appendix A. The MD graphical

processing unit package RUMD [33] was used to perform the calculation in double precision. The time step is equal to $\delta t = 0.86$ fs. Each simulation was equilibrated for a period of 1.7 ns and lasted thereafter 6.9 ns. Depending on the strain rate and the temperature, 8 or 16 independent initial configurations were used. The change in density from one initial configuration to the other is less than 10^{-12} %. The averages and standard errors shown in this paper correspond to the averages and standard errors over these independent simulations.

III. RHEOLOGY

Four main rheological properties can be computed from the NEMD simulations under shear. They are the shear viscosity η , the first and second normal stress coefficients Ψ_1 and Ψ_2 , and the non-equilibrium molecular pressure P . They provide information about the Newtonian and non-Newtonian behavior of the fluid.

These quantities are derived from the molecular stress tensor $\boldsymbol{\sigma}$, given by the Irving-Kirkwood formula [34]:

$$\boldsymbol{\sigma} = -\frac{1}{V} \left\langle \sum_{i=1}^{N_m} \frac{\mathbf{p}_i \mathbf{p}_i}{M_i} + \sum_{i=1}^{N_m} \sum_{j>i}^{N_m} \mathbf{r}_{ij} \mathbf{F}_{ij} \right\rangle, \quad (5)$$

where V is the volume of the system, $\langle \cdot \rangle$ denotes a time average over the non-equilibrium steady state, $\mathbf{r}_{ij} = \mathbf{r}_i - \mathbf{r}_j$ is the vector between the centers of mass of molecules i and j , $\mathbf{F}_{ij} = \sum_{\alpha} \sum_{\beta} \mathbf{F}_{i\alpha j\beta}$ is the intermolecular force acting on molecule i due to molecule j and $\mathbf{F}_{i\alpha j\beta}$ is the force acting on particle α in molecule i due to particle β in molecule j .

A. Shear viscosity

Due to the shear geometry enforced in the simulation, the shear viscosity is given by:

$$\eta = \frac{\sigma_{xy} + \sigma_{yx}}{2\dot{\gamma}}, \quad (6)$$

where $\dot{\gamma}$ is the shear rate. The variation of the viscosity η with the shear rate $\dot{\gamma}$ is plotted in Fig. 2 for different temperatures. At all temperatures the viscosity is

decreasing with increasing shear rate and the Coocoe bitumen is consequently a shear-thinning fluid. This is consistent with most experimental data on bitumen [6, 8, and 9]. However, bitumen has a broad range of behavior with shear rate and can also be shear-thickening [7]. Moreover, the higher the temperature, the higher the shear rate at which the fluid enters the Newtonian regime in the Coocoe model. Thus, the Newtonian plateau is clearly visible at temperature 603 K and barely noticeable at temperature 377 K in the range of shear rates accessible to NEMD simulations. In other words, over the whole range of shear rates spanned, the change in viscosity is larger at low temperatures than at high temperatures. This is in agreement with the experimental literature [6], stating a more pronounced non-Newtonian behavior of bitumen at low temperatures.

The zero shear rate viscosity η_0 can be determined using two empirical models to fit the data. The models are known as the Carreau-Yasuda model [35] and the Cross model [36]. The Carreau-Yasuda model suggests the following expression for the variation of viscosity with shear rate: $\eta = \eta_0/[1 + (\lambda\dot{\gamma})^2]^p$, where λ is a time constant and p a power law exponent. The Cross model suggests a different empirical expression for the variation of viscosity with shear rate: $\eta = \eta_\infty + (\eta_0 - \eta_\infty)/[1 + (K\dot{\gamma})^m]$, where η_∞ is the shear viscosity at infinite shear rate, K the consistency index, and m a power law exponent. The values of the parameters corresponding to the Carreau-Yasuda and Cross models are given in Tables I and II for all temperatures. The values of the zero shear rate viscosity η_0 should be taken with care for the two lowest temperatures as the Newtonian regime is not clearly visible.

The values of these different parameters will now be discussed. Both models obtain similar values for the viscosity at zero shear rate, which gives some confidence in the quality of the data. The experimental values for the zero shear rate viscosity at a given temperature depend a lot on the precise origin and age of the bitumen mixture studied. At around 377 K the experimental values for the viscosity can vary from 0.1 Pa·s [7] to more than 100 Pa·s [6 and 16]. The value found in this work around 0.1 Pa·s at 377 K is consequently at the lowest end of the broad range obtained experimentally for different bitumen mixtures.

T [K]	η_0 [Pa·s]	λ [s]	p
377	0.10	2.9×10^{-8}	0.29
452	0.022	2.7×10^{-8}	0.21
528	0.0055	2.6×10^{-8}	0.13
603	0.0016	6.7×10^{-9}	0.09

TABLE I. Values of parameters η_0 , λ , and p from the Carreau-Yasuda formula, for different temperatures T .

The values of the time constant λ in the Carreau-Yasuda model and of the consistency index K in the Cross model are also quite close to each other. They can be interpreted as the longest rotational relaxation time in the system [27]. The rotational relaxation time of the asphaltene molecules was estimated at temperature 452 K and density $964 \text{ kg}\cdot\text{m}^{-3}$ at equilibrium in an earlier work [18]. It was evaluated as the time needed for the rotational correlation function to decay to 0.75 and was found to be equal to $\tau_{\text{rot}} = 1.8 \times 10^{-8}$ s. This value is very close to the value of the time constants $\lambda = 2.7 \times 10^{-8}$ s and $K = 3.4 \times 10^{-8}$ s found at the same temperature and density in this work from the Carreau-Yasuda and Cross fits, respectively.

Finally, the Cross model does not seem to fit the data as well as the Carreau-Yasuda model for high shear rates, despite that the former model was designed to improve the fit at high shear rates by introducing a viscosity at infinite shear rate η_∞ . The fact that the viscosity keeps decreasing even at very high shear rates will be explained in terms of molecular aggregation in Sec. IV A.

To extrapolate the data to experimentally relevant temperatures around 300 K, we compare the variation of the zero shear rate viscosity with temperature to an Arrhenius behavior. The Arrhenius equation of the form $\eta_0(T) = \eta^\infty \exp(E/(k_B T))$, where η^∞ is the viscosity at infinite temperature and E the activation energy, is usually valid for a range of temperatures well above the glass transition [37]. Experimentally, the glass transition of bitumen depends on its exact composition and is typically around 250 K [38], which is well below the temperature range used in

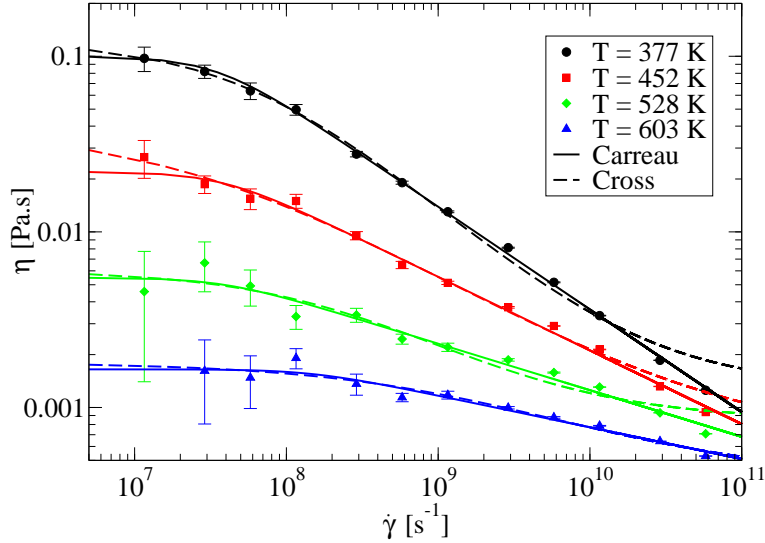


FIG. 2. (Color online) Variation of shear viscosity η with the shear rate $\dot{\gamma}$ for different temperatures. The viscosity values corresponding to the four lowest shear rates at temperature 603 K and 528 K were averaged over 16 independent simulations, whereas the other data points were averaged over 8 independent simulations. The value of the viscosity at the lowest shear rate and at temperature 603 K is not displayed because it is negative with an error bar larger than its absolute value.

T [K]	η_0 [Pa·s]	K [s]	η_∞ [Pa·s]	m
377	0.13	1.6×10^{-8}	0.0013	0.79
452	0.040	3.4×10^{-8}	0.00064	0.55
528	0.0061	4.2×10^{-9}	0.00085	0.70
603	0.0018	6.2×10^{-10}	0.00040	0.56

TABLE II. Values of parameters η_0 , K , η_∞ , and m from the Cross formula, for different temperatures T .

this work. The Arrhenius equation has been shown to fit the variation of the experimental zero shear rate viscosity with temperature quite well for some bitumen in a temperature range going from 273 to 363 K [8]. The variation with temperature

of the zero shear rate viscosity obtained with the Carreau-Yasuda and Cross fits is compared to an Arrhenius behavior in the inset of Fig. 3. Both sets of values follow an Arrhenius behavior. The parameters of the Arrhenius fit are found to be $E/k_B = 4073$ K and $\eta^\infty = 2.27 \times 10^{-6}$ Pa·s for the Carreau-Yasuda set of data and $E/k_B = 4245$ K and $\eta^\infty = 2.00 \times 10^{-6}$ Pa·s. Taking into account the data from the Carreau-Yasuda fit, the Arrhenius equation predicts a value for the viscosity of 2.5 Pa·s at 293 K. Again, it is at the lowest end of the broad range of experimental values for the zero shear rate viscosity at this temperature. These values can range from 1 Pa·s [4] up to $10^4 - 10^6$ Pa·s [5, 8, 9, and 16].

The fact that the viscosity of the Cooe bitumen is quite low compared to experimental viscosities of bitumen at ambient pressure and temperature can be related to the observation that the density of the Cooe bitumen is itself quite different from experimental densities. At a temperature of 377 K, the density of the Cooe bitumen is $1007 \text{ kg}\cdot\text{m}^{-3}$. It is to be compared with the thorough experiments carried out on Athabasca bitumen [39] which find a linear dependency of bitumen density on temperature at ambient pressure. Extrapolating their results to 377 K leads to a bitumen density around $955 \text{ kg}\cdot\text{m}^{-3}$, which is significantly lower than the density of the Cooe bitumen at the same pressure and temperature. This difference between the equation of state of our model and the equation of state obtained experimentally could be due to the specific type of asphaltene molecules that we chose. It has very short alkyl chains aside from the aromatic plane compared to the resin molecule. We know from a previous work [18], that adding resin molecules while removing asphaltene molecules from the mixture has a tendency to lower the density at constant pressure. Thus, considering asphaltene molecules with longer alkyl chains could lower the density of the model and could also change the viscosity. In the future, we plan to investigate this possible effect of the length of the alkyl chains on the density and viscosity of the mixture by comparing two mixtures with alkyl chains of different lengths.

In an attempt to extrapolate not only the zero shear rate viscosity but also the shear rate dependent viscosity to ambient temperature, we tested the time-temperature superposition principle. This principle has been shown to be generally

valid experimentally [40] and is also discussed in another numerical model of bitumen [41]. The reduced viscosity and reduced shear rate are defined as η/a_η and $\dot{\gamma}a_T$, respectively, where

$$a_\eta = \frac{\eta_0(T, \rho)}{\eta_0(T_{\text{ref}}, \rho_{\text{ref}})}, \quad (7)$$

$$a_T = a_\eta \frac{T_{\text{ref}} \rho_{\text{ref}}}{T \rho}. \quad (8)$$

The zero shear rate viscosity η_0 is chosen from the Carreau-Yasuda fit, the reference temperature T_{ref} and the reference density ρ_{ref} are chosen to be 603 K and 833 kg·m⁻³ respectively, because the Newtonian regime at this state point is the most clearly defined. The procedure to obtain the reduced viscosity and reduced shear rate is described in Ref. [42] and its theoretical foundation is discussed in Ref. [35]. In particular, the time temperature superposition principle can be shown to be valid if all the relaxation times in the system have the same temperature dependence [43]. Figure 3 shows the variation of the reduced viscosity η/a_η with the reduced shear rate $\dot{\gamma}a_T$ for the Cooee bitumen. The time temperature superposition principle is not so well satisfied for this model bitumen.

To explain this fact, we tried first to take into account the colloidal nature of bitumen [11]. Indeed, the Cooee bitumen mixture can be seen as a suspension of branched nanoaggregates composed of aromatic molecules and surrounded by a saturated hydrocarbon solvent [18 and 29]. In the experimental literature, bitumen mixtures are also sometimes treated as colloidal suspensions, because the typical size of a nanoaggregate is generally agreed to be around 2 nm [11]. In the case of a dilute or semidilute suspension, the contribution of the suspended objects to the total viscosity can be well approximated by subtracting the pure solvent viscosity to the total viscosity. In the case of the Cooee bitumen studied here, the volume fraction of aromatic molecules involved in the nanoaggregates is $\phi = 0.42$, far from the dilute limit. We tried nevertheless to subtract the viscosity of the pure solvent at the same temperature and same density from the viscosity of the bitumen mixture, to see if the time temperature superposition principle was better satisfied. The reduced viscosity is now equal to $(\eta - \eta_s)/a'_\eta$ and the reduced shear rate to $\dot{\gamma}a'_T$, where η_s is the pure solvent viscosity at the same temperature and density and

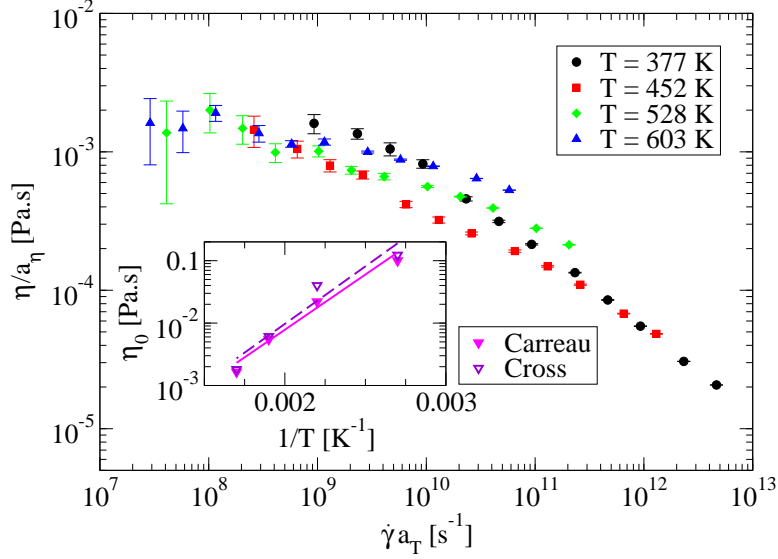


FIG. 3. (Color online) Variation of the reduced viscosity η/a_η with the reduced shear rate $\dot{\gamma}a_T$ for different temperatures. This is a test of the time-temperature superposition principle. Inset: (Color online) Variation of the zero shear viscosity η_0 , evaluated from both the Carreau-Yasuda and the Cross models, with the inverse temperature. The solid lines are Arrhenius fits to the data.

where a'_η and a'_T are given by:

$$a'_\eta = \frac{\eta_0(T, \rho) - \eta_s(T, \rho)}{\eta_0(T_{\text{ref}}, \rho_{\text{ref}}) - \eta_s(T_{\text{ref}}, \rho_{\text{ref}})}, \quad (9)$$

$$a'_T = a'_\eta \frac{T_{\text{ref}} \rho_{\text{ref}}}{T \rho}. \quad (10)$$

The reduced viscosity is plotted versus the reduced shear rate in Fig. 4, for the three highest temperatures. As expected, subtracting the solvent does not help the time superposition principle to be satisfied. Rather than a solvent effect, the failure of the time superposition principle will be related to the presence of at least two characteristic times related to the nanoaggregates and with *a priori* different temperature dependences in Sec. IV A. The inset of Fig. 4 displays the variation of the viscosity of the pure solvent with shear rate for different temperatures. It can be seen that at the lowest temperature, the pure solvent never reaches the Newtonian plateau. It actually crystallizes. This crystallization is not seen in the bitumen

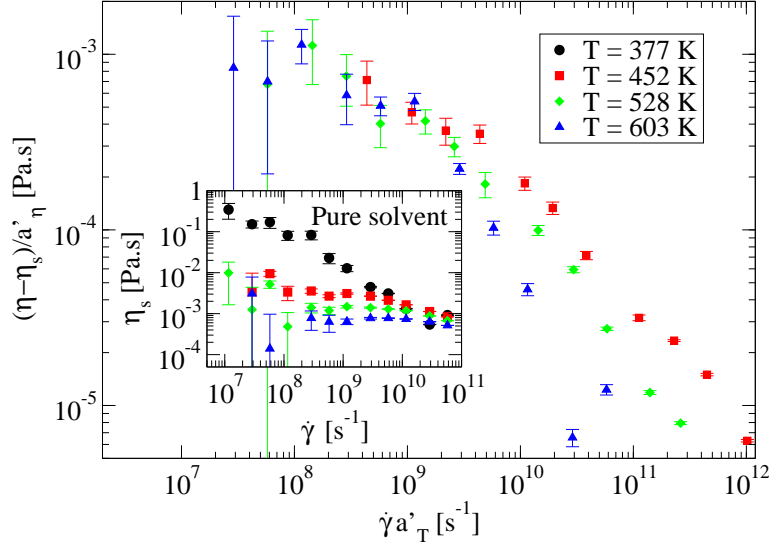


FIG. 4. (Color online) Variation of the reduced viscosity $(\eta - \eta_s)/a'_\eta$ with the reduced shear rate $\dot{\gamma}a'_T$ at different temperatures. Inset: Variation of the viscosity η_s with the shear rate $\dot{\gamma}$ at different temperatures for the pure solvent.

mixture. There could be two main reasons behind this: the melting temperature of the mixture is lower than that of the pure solvent ; the bitumen mixture is blocked in a metastable liquid state or a glassy state during the time spans accessible to MD whereas the pure solvent is not. Regardless of the possible crystallization of the solvent at the lowest temperature, the fact that the bitumen mixture is so far from the dilute limit indicates strongly that aggregate-aggregate interactions are very important to understand the rheology of the mixture.

B. Normal stress coefficients

A fluid in the non-Newtonian regime is also characterized by shear-rate dependent normal stress coefficients. To first order in the shear rate, the two normal stress differences $\sigma_{xx} - \sigma_{yy}$ and $\sigma_{yy} - \sigma_{zz}$ are exactly zero because a shear strain does not cause any change in the diagonal components of the stress tensor. Different models and experiments on polymers show that the first departures of the normal stress differences from zero occur at second order in the strain rate [10]. Therefore, the

T [K]	α	β
377	1.4	1.4
452	1.2	1.1
528	0.98	0.81
603	0.96	0.71

TABLE III. Values of exponents α and β describing the power law decay of the normal stress coefficients Ψ_1 and Ψ_2 , respectively, for different temperatures T .

normal stress coefficients Ψ_1 and Ψ_2 are defined as: $\Psi_1 = (\sigma_{xx} - \sigma_{yy})/\dot{\gamma}^2$ and $\Psi_2 = (\sigma_{yy} - \sigma_{zz})/\dot{\gamma}^2$. Thus, at low shear rates, the normal stress coefficients Ψ_1 and Ψ_2 should plateau to a given value. At larger shear rates, the normal stress coefficients are known to decrease for polymers [10]. The normal stress coefficients Ψ_1 and Ψ_2 obtained from the NEMD simulations of Coocoe bitumen are shown in Fig. 5 (a) and (b), respectively. Only the results having a standard error lower than their absolute value are displayed. The first normal stress coefficient Ψ_1 decreases with increasing shear rate $\dot{\gamma}$, showing again that bitumen has reached a non-Newtonian regime in the range of shear rates spanned in the simulations. The second normal stress coefficient Ψ_2 has been less studied, but is usually negative in experiments on polymer fluids [25 and 35]. The simulations presented in this paper also find a negative second normal stress coefficient Ψ_2 . The absolute value of the second normal stress coefficient Ψ_2 decreases with increasing shear rate, which is also a signature of the non-Newtonian regime. The decrease of the two normal stress coefficients in the non-Newtonian regime can be fitted to a power law [25]: $\Psi_1 \sim \dot{\gamma}^{-\alpha}$ and $-\Psi_2 \sim \dot{\gamma}^{-\beta}$ for the coefficients Ψ_1 and Ψ_2 , respectively. The values of the exponents α and β are displayed in Table III. They are close to each other and decrease with increasing temperature, reaching a value lower than 1 at the highest temperatures.

Finally, the normal stress ratio $-\Psi_2/\Psi_1$ is plotted versus shear rate in Fig. 5 (c). This ratio is known to be equal to 0.24 for linear polymer melts and to 0.3 for branched polymer melts [10]. In the case of bitumen, it is higher, around 0.5, but

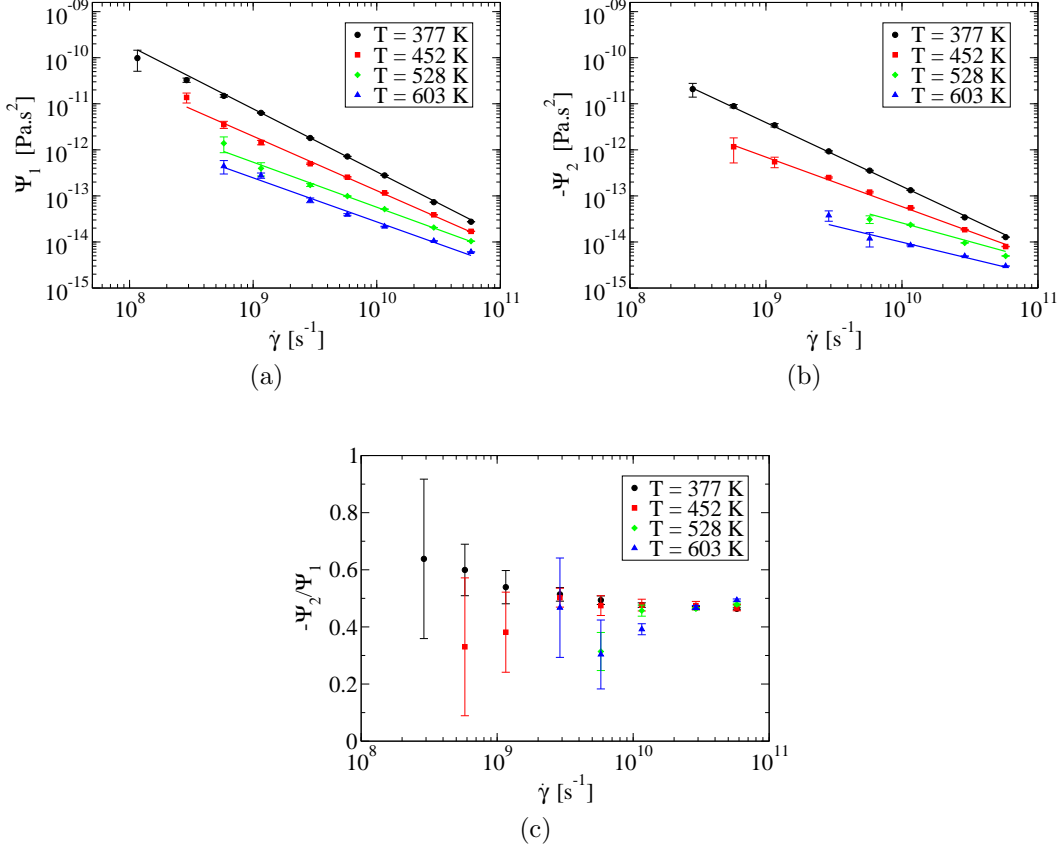


FIG. 5. (Color online) (a) and (b): Variation of the first Ψ_1 and second Ψ_2 normal stress coefficients with the shear rate $\dot{\gamma}$ for different temperatures, respectively. In (b) $-\Psi_2$ is plotted versus shear rate. The straight lines are power law fit to the data. Their exponents are given in Table III. (c): Variation of the ratio $-\Psi_2/\Psi_1$ with the shear rate $\dot{\gamma}$ for the same temperatures.

does not seem to depend on either shear rate or temperature. This value of the normal stress ratio $-\Psi_2/\Psi_1$ will be related to an anisotropy effect in Sec. IV B 1.

C. Pressure

The pressure of the system is defined as minus a third of the trace of the molecular stress tensor given in Eq. (5). For simple fluids, the pressure P has been shown to have a power law dependency on shear rate [44 and 45]: $P = P_0 + b\dot{\gamma}^\epsilon$, where P_0 is the pressure at equilibrium. For more complex fluids in particular for linear polymer

T [K]	ϵ
377	0.86
452	1.4
528	1.9
603	2.2

TABLE IV. Values of the exponent ϵ describing the power law increase of the normal isotropic pressure P for different temperatures T .

melts, the pressure begins to decrease with increasing shear rate before increasing with a power law behavior [46]. The variation of the pressure with the shear rate is displayed in Fig. 6 for the Cooe bitumen model. The variation is found to be monotonic with the shear rate for the range of temperatures explored. It can be fitted quite well with a power law. The exponent of the power law is given for each temperature in Table IV. The observation that the pressure is monotonically increasing with the shear rate instead of having a clear minimum could be due to the fact that the molecules in bitumen are not all linear. Moreover, it is known that the pressure increases faster with shear rate for high generation dendrimers than for linear polymers [46]. This fast increase can mask the local minimum of the pressure. The same mechanism could be at play in the bitumen mixture studied here.

Figure 6 also shows that the density of the mixture at each temperature is chosen so that the equilibrium pressure P_0 is around the atmospheric pressure.

Finally, for shear rates lower than $3 \times 10^8 \text{ s}^{-1}$ and for all temperatures, the pressure does not deviate significantly from its equilibrium value, enabling a direct comparison with experimental results, usually obtained at constant pressure.

IV. MOLECULAR STRUCTURE

As mentioned in Sec. II A, the Cooe bitumen model used in this paper contains four molecule types. In order of increasing molecular weight, these types are: docosane, resinous oil, resin and asphaltene. Of these, only the docosane molecules

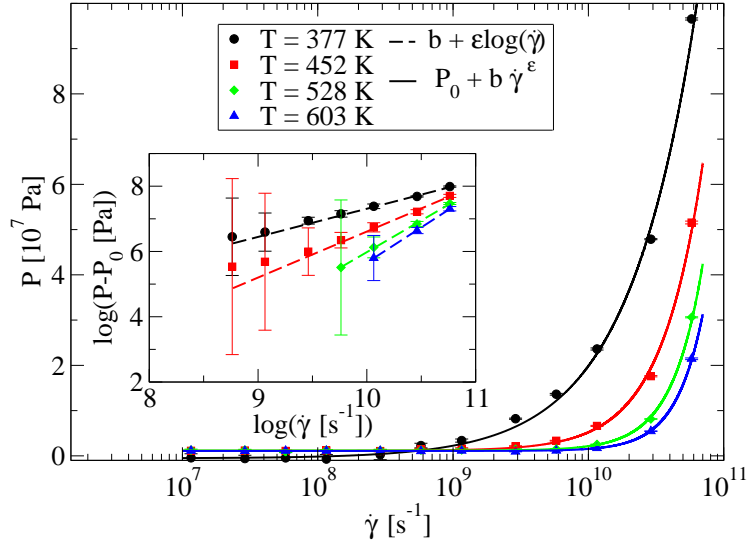


FIG. 6. (Color online) Variation of the normal isotropic pressure P with the shear rate $\dot{\gamma}$ for different temperatures. Inset: Variation of $\log(P - P_0)$ with $\log(\dot{\gamma})$. Only data with error bars lower than the value of $\log(P - P_0)$ are shown. The dashed lines are straight line fits to this data. The solids lines in the main figure correspond to equation $P = P_0 + b\dot{\gamma}^\epsilon$, where b and ϵ were determined by the straight line fits to $\log(P - P_0)$ versus $\log(\dot{\gamma})$. The exponents ϵ are given in Table IV.

are not aromatic. This composition resembles the SARA classification [31] and is able to reproduce the characteristic supramolecular structure of bitumen in nanoaggregates [11]. The nanoaggregates are composed of the aromatic molecules aligned with respect to each other. An example of a nanoaggregate seen in the simulations is shown in Fig. 7. The docosane molecules can be seen as a solvent for the nanoaggregates. The aim of this section is to quantify the variation of the nanoaggregate structure and of the inter- and intramolecular structures of each molecule type with shear rate and temperature as well as to compare it with the variation of the rheological properties obtained in Sec. III.

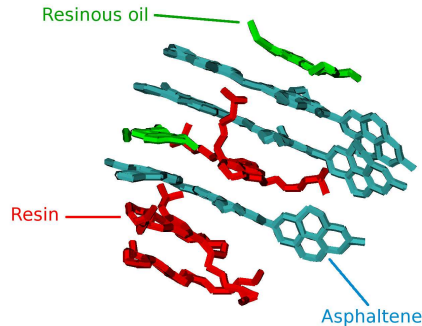


FIG. 7. (Color online) Snapshot of a linear nanoaggregate, obtained in equilibrium molecular dynamics. Asphaltene molecules are in blue, resin molecules in red and resinous oil molecules in green. Modified with permission from *J. Chem. Phys.* **141**, 144308 (2014).

A. Nanoaggregate size

The definition of a nanoaggregate from a molecular point of view is described in detail in Refs. [18 and 29] for equilibrium simulations. The nanoaggregates are composed of all the aromatic molecules and are branched. The branched structure arises from the asphaltene molecules having two flat parts, a head and a body, oriented in different directions. Each part can align to other flat aromatic molecules creating a branched structure [18]. In this work, we focus on the linear segments of these branched structures, because their size distribution has been studied in detail at equilibrium in an earlier work [29], but the presence of the branched structure should be kept in mind. The definition of a linear segment sums up to the following rule: two aromatic molecules are nearest neighbors in the same nanoaggregate if they are “well-aligned” and “close enough”. Only the alignment of aromatic molecules to an asphaltene body and not to an asphaltene head is considered here, to extract purely linear structures. All molecules connected by this rule are part of the same linear nanoaggregate. The same rule was used in the NEMD simulations and the average number of aromatic molecules in a linear nanoaggregate could be quantified for different shear rates. The results are plotted in Fig. 8 (a) for all temperatures.

The variation of the nanoaggregate size with the shear rate at a fixed temperature

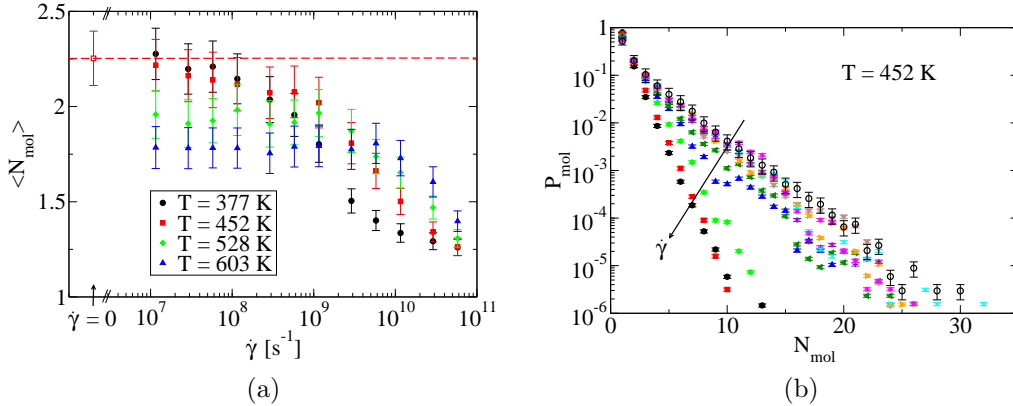


FIG. 8. (Color online) (a): Variation of the average number of aromatic molecules $\langle N_{\text{mol}} \rangle$ in a linear nanoaggregate with the shear rate $\dot{\gamma}$ for different temperatures. The open symbol and the dashed line represent the corresponding value at equilibrium and at temperature 452 K. (b): Probability P_{mol} to have a linear nanoaggregate containing N_{mol} molecules versus N_{mol} at temperature 452 K and for different shear rates from 6×10^7 to $10 \times 10^{10} \text{ s}^{-1}$ (the two lowest shear rates are omitted for the sake of clarity). The open symbols correspond to the same result at equilibrium.

is first considered. At low shear rates, the size of the nanoaggregates is close to their size at equilibrium as is shown for temperature 452 K in Fig. 8 (a). The full distribution of the number of aromatic molecules in a linear nanoaggregate at low shear rates is also very close to the same distribution at equilibrium as can be seen in Fig. 8 (b). At these low shear rates, the size distribution has a biexponential shape, which we attributed, in a previous work [29], to longer nanoaggregates being less bent and containing more asphaltene molecules than smaller ones. After a plateau at low shear rates, the nanoaggregate size decreases quite sharply with increasing shear rate until it reaches a value close to 1, indicating that nearly all nanoaggregates are reduced to single molecules. In other words, the shear flow induces nanoaggregate rupture. Figure 8 (b) shows that at the highest shear rate and at temperature 452 K some longer nanoaggregates still remain but with a low probability. Interestingly, figure 8 (b) also shows that at high shear rates the size distribution is closer to a single exponential distribution. However, no noticeable variation of the relative composition of the nanoaggregates with their size was seen when the shear rate is

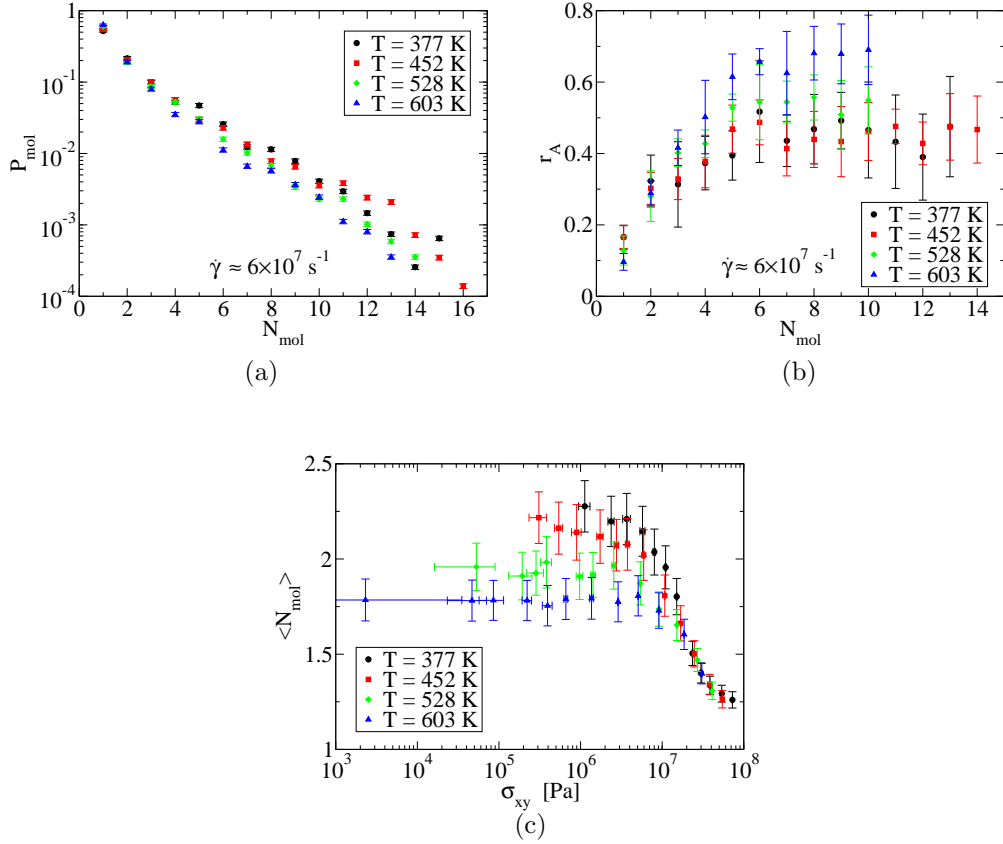


FIG. 9. (Color online) (a): Same as Fig. 8 (b) for a given shear rate of $6 \times 10^7 \text{ s}^{-1}$ and at different temperatures. (b): Variation of the fraction r_A of asphaltene molecules in a nanoaggregate with the number N_{mol} of aromatic molecules in the same nanoaggregate, at different temperatures and at a fixed shear rate of $6 \times 10^7 \text{ s}^{-1}$. (c): Variation of the average number of aromatic molecules $\langle N_{\text{mol}} \rangle$ in a linear nanoaggregate with the stress σ_{xy} for different temperatures.

increased (not shown).

The variation of the linear nanoaggregate size with temperature at a fixed shear rate is now considered. As can be seen in Fig. 8 (a), the nanoaggregate size at low shear rates decreases with increasing temperature. The size distribution of the linear nanoaggregates at a given low shear rate appears biexponential at all temperatures as can be seen in Fig. 9 (a). The cause of the decrease of the nanoaggregate size with temperature at low shear rates can be further investigated by looking at the relative composition of the nanoaggregates for different temperatures. The fraction r_A

of asphaltene molecule in a nanoaggregate is defined as the number of asphaltene molecules in this nanoaggregate divided by the total number of aromatic molecules in the same nanoaggregate. Figure 9 (b) shows the variation of the fraction r_A of asphaltene molecules with the nanoaggregate size for different temperatures and at a low shear rate of $6 \times 10^7 \text{ s}^{-1}$. For linear nanoaggregates with a number of molecules larger than 3, the fraction r_A of asphaltene molecules in the nanoaggregates increases with increasing temperature. Concurrently, the fraction of resin and resinous oil molecules in the nanoaggregates tends to decrease with increasing temperature in long nanoaggregates. It means that the overall decrease of the nanoaggregate size with temperature is mainly due to resin and resinous oil molecules being excluded from the aggregates at large temperatures. The asphaltene molecules stay aggregated even at large temperatures. It is probably an effect of the cohesive energy being higher in absolute value between two asphaltene molecules than between two resin or two resinous oil molecules. This is itself due the difference in the sizes of the aromatic structures. Asphaltene molecules have a larger aromatic structure than resin and resinous oil molecules, thus creating a larger π -stacking interaction between the aromatic planes of two asphaltene molecules than between two resin or resinous oil molecules. At high shear rates in Fig. 8 (a), it seems on the contrary that the nanoaggregate size increases with increasing temperature. It is due to the fact that the shear rate at which the nanoaggregates begin to break up is not the same at all temperatures. The higher the temperature, the lower the shear rate needed to break up the nanoaggregates. This apparent crossover between the curves giving the nanoaggregate size versus the shear rate at different temperatures can be removed if the average nanoaggregate size is plotted versus the shear stress σ_{xy} rather than the shear rate $\dot{\gamma}$. This can be seen in Fig. 9 (c). This figure also shows that above a certain shear stress, all curves collapse. Figure 9 (c) can be understood if one assumes that the size of the nanoaggregates depends on two factors: the thermal energy and the work done by the external shear force applied to the system. The thermal energy is directly proportional to temperature and the work done by the shear force can be estimated from the product of the shear stress σ_{xy} and the characteristic volume of an aromatic molecule in a nanoaggregate. At low shear stresses,

the work done by the shear force is negligible with respect to the thermal energy and the nanoaggregate size is determined by thermal energy alone. The nanoaggregates have then their equilibrium size. At high shear stresses, on the contrary, the thermal energy is negligible with respect to the work done by the shear force and the nanoaggregate size is determined by the shear stress σ_{xy} alone. The curves at different temperatures collapse at high shear stresses. At intermediate values of the shear stress, both factors play a role in the nanoaggregate size. In this intermediate regime, an increase in shear stress at constant temperature results in a monotonic decrease of the nanoaggregate size and an increase in temperature at constant shear stress results in a monotonic decrease of the nanoaggregate size.

The connection between the rupture of the nanoaggregates around a given shear rate and the variation of the viscosity with shear rate and temperature quantified in Sec. III is now discussed. The overall decrease of the nanoaggregate size with increasing temperature at low shear rates contributes to the decrease of the viscosity observed with increasing temperature in Fig. 2.

The rupture of the nanoaggregates at high shear rates is consistent with a decrease in the viscosity at these same shear rates instead of a plateauing around the viscosity at infinite shear rate η_∞ , predicted by the Cross model. The Carreau-Yasuda model does not postulate the existence of a constant viscosity at infinite shear rate. It could be why it better fits the data than the Cross model, as was found in Sec. III.

Moreover, the important change in the nanoaggregate size upon shearing could explain why the time-temperature superposition principle is not satisfied. Indeed, the time temperature superposition typically works when all relaxation times have the same temperature dependence [43]. In the case of the Coovee bitumen model, at least two main long relaxation times can be identified: the rotational relaxation time of the asphaltene molecules, close to the characteristic time λ of the Carreau-Yasuda fit, and the inverse shear rate at which the nanoaggregates rupture. They have *a priori* different temperature dependences, which could explain why the time temperature superposition principle is not satisfied.

B. Molecular alignment

The variation of the size of the nanoaggregates, a supramolecular structure specific to bitumen, has been addressed in Sec. IV A. This section (IV B) and the next (IV C) are devoted to more usual quantifications of the variation of the inter- and intramolecular structures with the shear rate and their link to the shear-thinning behavior reported in Sec. III. This section focuses on the alignment of the molecules in the flow direction, also known as form birefringence.

Form birefringence is a departure from the isotropic equilibrium state of the fluid due to the applied velocity gradient. The anisotropy arises in this case from the alignment of the molecules in the flow direction [47]. The form birefringence is quantified using a molecular order tensor \mathbf{S}_m , defined for a given molecule type as:

$$\mathbf{S}_m = \frac{1}{N_m} \sum_{i=1}^{N_m} \left\langle \mathbf{u}_i \otimes \mathbf{u}_i - \frac{1}{3} \mathbf{I} \right\rangle, \quad (11)$$

where N_m is the total number of molecules of the considered type, \mathbf{u}_i is the unit vector denoting the principal direction of molecule i of the given type, \mathbf{I} is the identity tensor, and $\langle \cdot \rangle$ denotes a time average in the non-equilibrium steady state. The principal direction \mathbf{u}_i of molecule i is the unit eigenvector corresponding to the largest eigenvalue of the gyration tensor \mathbf{R}_g^2 , defined as:

$$\mathbf{R}_g^2 = \frac{1}{2N_i} \sum_{\alpha=1}^{N_i} \sum_{\beta=1}^{N_i} (\mathbf{r}_\alpha - \mathbf{r}_\beta) \otimes (\mathbf{r}_\alpha - \mathbf{r}_\beta), \quad (12)$$

where N_i is the number of atoms in molecule i and \mathbf{r}_α is the position of atom α in molecule i . Once the molecular order tensor \mathbf{S}_m is determined for each molecule type, two quantities derived from it are of interest: the molecular order parameter S_m and the molecular alignment angle χ_m . The molecular order parameter S_m is defined as 3/2 times the largest eigenvalue of the molecular order tensor. It is equal to 0 when the molecules are randomly oriented and to 1 when all molecules are perfectly aligned. The molecular alignment angle χ_m is equal to $\arctan(e_y/e_x)$, where $\mathbf{e} = (e_x, e_y, e_z)$ is the eigenvector corresponding to the largest eigenvalue of the molecular order tensor \mathbf{S}_m . The molecular alignment angle χ_m represents the angle between the average molecular orientation \mathbf{e} and the shear direction (x -direction in this case) in the xy -plane.

1. *Molecular order parameter*

The variation of the molecular order parameter S_m with the shear rate $\dot{\gamma}$ is displayed in Fig. 10 (a) for a temperature of 452 K and for the different molecule types. The curves are quite different from one molecule type to another. For docosane molecules, the molecular order parameter S_m tends to zero in the limit of vanishing shear rate. This behavior is expected, since the docosane molecules are isotropically distributed at equilibrium. The molecular order parameter for docosane increases monotonically to reach the value 0.55 at the highest shear rate simulated, showing an alignment of docosane molecules in the shear direction. This is consistent with the shear thinning behavior globally observed for Coocoe bitumen [48]. For asphaltene, resin and resinous oil molecules the curve is qualitatively different. At low shear rates, until a critical shear rate of approximately $\dot{\gamma}_c = 2 \times 10^9 \text{ s}^{-1}$ at temperature 452 K is reached, the molecular order parameter of the three aromatic types is roughly constant and non-zero. Above this critical shear rate, the molecular order parameter begins to increase with the shear rate. The small finite value reached by the molecular order parameter at low shear rates is equal to the one obtained from equilibrium molecular dynamics simulations, as can also be seen in Fig. 10. This value is higher for asphaltene molecules than for resinous oil molecules and for resin molecules. This unusual behavior of the molecular order parameter is easily explained if the presence of nanoaggregates at low shear rates is considered. Indeed, the long nanoaggregates tend to align with respect to each other, due to steric hindrance, creating a slight anisotropy in the system. This anisotropy is also present at equilibrium. At equilibrium, it was previously determined [29] that long nanoaggregates contain more asphaltene molecules than resinous oil molecules and that the resin content is the smallest. This explains why the anisotropy is larger for asphaltene molecules than for resinous oil molecules and the smallest for resin molecules. According to Fig. 8 (a), at temperature 452 K, the nanoaggregates begin to break up at a shear rate very close to the critical shear rate $\dot{\gamma}_c = 2 \times 10^9 \text{ s}^{-1}$. This indicates that the increase of the molecular order parameter for shear rates higher than $\dot{\gamma}_c$ is due to the alignment of the single molecules in the flow direction. Again, this is consistent with the shear thinning behavior observed at high shear rates.

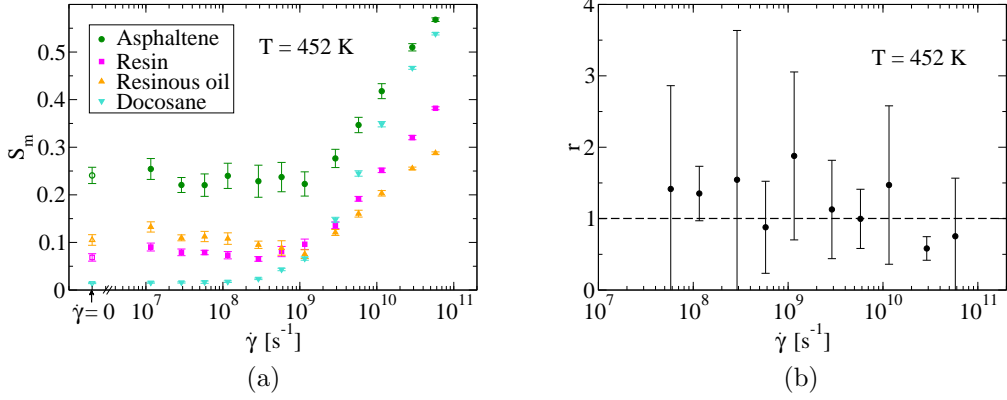


FIG. 10. (Color online) (a): Variation of the molecular order parameter S_m with shear rate $\dot{\gamma}$ for different molecule types and for a temperature of 452 K. The open symbols represent the corresponding values at equilibrium. (b): Variation of the ratio $r = s_{\text{rot}}/s_{\text{conf}}$ comparing the standard deviation due to the anisotropy of the sample to the standard deviation due to different samples with the shear rate $\dot{\gamma}$ at a temperature of 452 K. The error bars are calculated for each type of standard deviations as the absolute value of the difference between the standard deviation corresponding to half of the data set and the standard deviation corresponding to the other half of the data set. The relative error on the ratio r is then calculated as the sum of the relative errors on s_{rot} and s_{conf} . The dashed line has equation $r = 1$ and corresponds to the anisotropy of the sample being the main source of variation between one initial configuration and another.

Moreover, the existence of this intrinsic anisotropy in the sample could explain why the value of the normal stress ratio $-\Psi_2/\Psi_1$ is different from what is found for linear or branched polymer melts. Indeed, the normal stress ratio $-\Psi_2/\Psi_1$ is a measure of the anisotropy between the xx - and zz - directions on the one hand and the xx - and yy - directions on the other hand, which can be influenced by an ordering of the system.

With the MD simulations which we carried out, we cannot know whether the global anisotropy of the system is a finite size effect or if it is also seen in macroscopic samples. In this last case, bitumen could resemble the nematic phase of a discotic liquid crystal, formed by the stacking of disk-shaped molecules [49]. Experimentally, it is known that there is a change of the supramolecular structure of

bitumen with the concentration of asphaltene molecules. At low concentrations, small and isotropically distributed nanoaggregates can be seen. At larger concentrations, the nanoaggregates gather in clusters. At even larger concentrations, the clusters are all connected to form a network [11]. This last stage could be representative of the simulations carried out in this work. The global anisotropy of the system was evaluated using a molecular order tensor \mathbf{Q} defined in a very similar way than the molecular order tensor S_m , specified for each molecule type in Eq. (11). The only differences are that the average is done over all aromatic molecules instead of over one particular type and that each molecule orientation is taken to be the unit vector normal to the molecule plane instead of the principal direction determined by the tensor of gyration. The molecular order parameter Q is then $3/2$ of the largest eigenvalue of the molecular order tensor \mathbf{Q} . It is found to be equal to $Q = 0.12 \pm 0.01$ at equilibrium [29]. This value of Q is sufficiently small, so that the shear viscosity can be treated as an isotropic scalar quantity.

To further investigate the effect of the anisotropy of the sample on the viscosity, simulations were performed in the same shearing geometry as before and with the same starting configurations except that the y - and z - coordinates are exchanged. The simulations were carried out at a temperature of 452 K for the same shear rates and the same density. The shear viscosity was analyzed and the following comparison was made. Let η_i and η'_i denote the viscosities of the system starting with configuration i and the corresponding rotated configuration, respectively. Let also $\bar{\eta}_i$ be the average $(\eta_i + \eta'_i)/2$. The standard deviation s_{rot} due to the anisotropy of the configuration is quantified as:

$$s_{\text{rot}} = \sqrt{\frac{1}{N_{\text{conf}}} \sum_{i=1}^{N_{\text{conf}}} (\eta'_i - \bar{\eta}_i)^2}, \quad (13)$$

where $N_{\text{conf}} = 8$ is the total number of initial configurations considered. A similar standard deviation s_{conf} comparing different initial configurations and not an initial configuration with a rotation of itself is defined as:

$$s_{\text{conf}} = \sqrt{\frac{1}{N_{\text{conf}}} \sum_{i \neq j} (\eta_i - (\eta_i + \eta_j)/2)^2}, \quad (14)$$

where i and j are two random different configurations, chosen from the 8 different

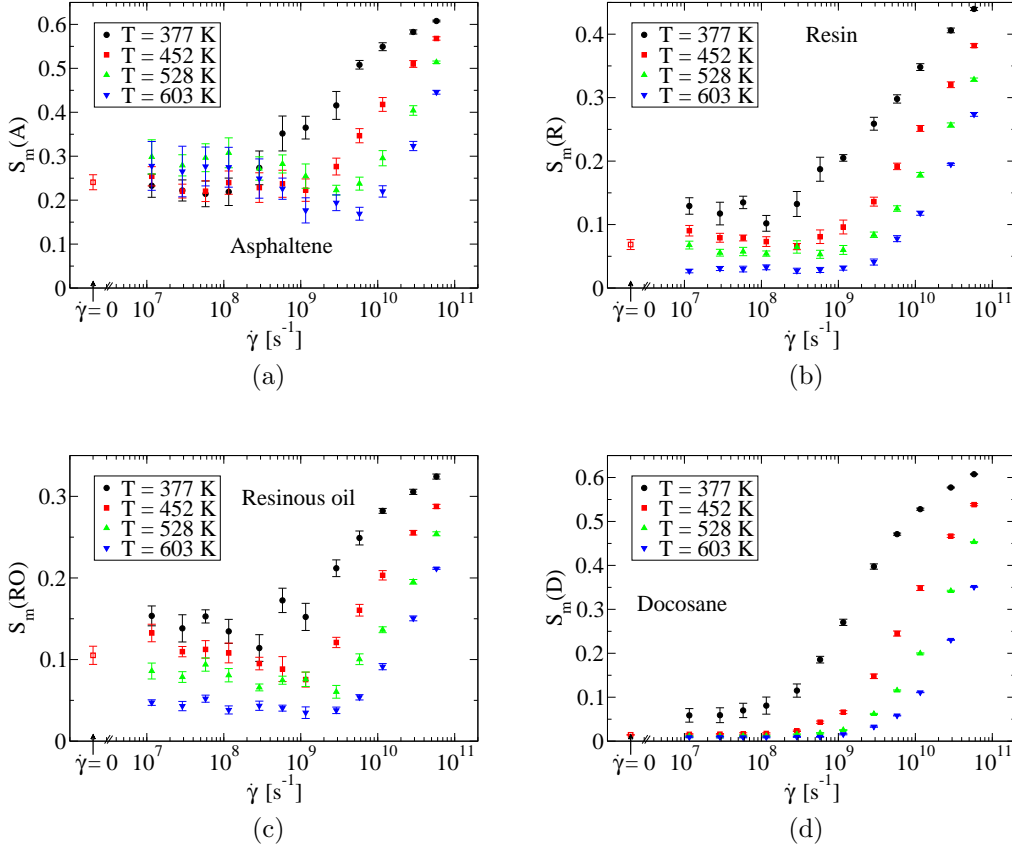


FIG. 11. (Color online) Variation of the molecular order parameter S_m with shear rate $\dot{\gamma}$ at different temperatures for asphaltene (a), resin (b), resinous oil (c) and docosane (d) molecules.

configurations available. Exactly N_{conf} pairs (i, j) are considered for the sake of symmetry with the definition of s_{rot} . The variation of the ratio $r = s_{\text{rot}}/s_{\text{conf}}$ with the shear rate is displayed in Fig. 10 (b). The ratio of the two standard deviations is around 1 for all shear rates indicating that the main source of difference between two configurations is the anisotropy of the sample. The values of the viscosity given in Fig. 2 should therefore be understood as an average viscosity over different orientations.

Figure 11 shows the variation of the molecular order parameter of the four different molecule types with shear rate for different temperatures. From Fig. 11, it is quite clear that for all molecule types, the molecular order parameter at a given high shear rate increases with decreasing temperature. This is due to the fact that

for a given shear rate at low temperatures the stress felt by the molecules is higher and the alignment in the direction of the flow is more pronounced than at high temperatures. At low shear rates, the behavior is quite different from one molecule type to another. For docosane molecules, the molecular order parameter $S_m(D)$ decreases with increasing temperature, for the same reason as at high shear rates. For resin and resinous oil molecules the molecular order parameter also decreases with increasing temperature at low shear rates. This is probably because as the temperature increases, the resin and resinous oil molecules are more often present as single molecules than in long nanoaggregates (see Fig 8 (d)), which reduces their global ordering. In contrast, asphaltene molecules stay in long nanoaggregates even at high temperatures and their molecular order parameter is nearly independent of temperature at low shear rates.

An interesting feature can be noticed for the molecular order parameter $S_m(A)$ of asphaltene molecules at high temperatures. Looking closely at the data of Fig. 11 (a) at temperature 603 K, one can note three different regimes with increasing shear rate: at low shear rates $S_m(A)$ is mostly constant, at intermediate shear rates $S_m(A)$ slightly decreases with the shear rate, and finally at large shear rates it increases. The intermediate shear rate range corresponds roughly to $[3 \times 10^8, 6 \times 10^9] \text{ s}^{-1}$ for temperature 603 K. At these shear rates, the average number of molecules in the nanoaggregates is still very close to its equilibrium value as can be seen in Fig. 8 (a). Consequently, the decrease in the molecular order parameter of the asphaltene molecules in this intermediate shear rate range can be interpreted in the following way: the nanoaggregates are still well formed, but the shear flow is strong enough to disturb the alignment of the nanoaggregates with respect to each other causing the order parameter to locally drop. At higher shear rates the nanoaggregates break, the molecules align in the shear direction and the molecular order parameter increases again. This intermediate drop of the molecular order parameter $S_m(A)$ of asphaltene molecules is also noticeable for temperature 528 K, but not for lower temperatures. It might be because the nanoaggregates break before the shear flow is strong enough to modify the alignment of the nanoaggregates with respect to each other. The direct consequence of this reorganization of the

nanoaggregates with respect to each other on the behavior of the viscosity with the shear rate is unclear. In total, the fluid is shear-thinning in this range of shear rates, as can be seen in Fig. 2. This global behavior could be mainly due to the alignment of the docosane molecules in the shear direction, the order parameter of the resin and resinous oil molecules being nearly constant in this range.

2. *Molecular alignment angle*

The variation of the molecular alignment angle χ_m is plotted for each molecule type versus the shear rate $\dot{\gamma}$ at temperature 452 K in Fig. 12 (a). The typical behavior for a polymer solution under shear is the following: in the Newtonian regime, the molecular alignment angle is around 45 degrees and in the non-Newtonian regime, the molecular alignment angle decreases until reaching zero. The value of 45 degrees is expected in the Newtonian regime, due to the nonuniform distribution of angular velocity of the molecules in the shear flow [25]. At larger shear rates, the molecules align to the shear flow resulting in a vanishing molecular alignment angle. This general behavior is roughly seen for all molecule types in Fig. 12 (a), though the error bars are very large at low shear rates. The large error bars at low shear rates can be explained by the fact that at these shear rates the nanoaggregates are well formed and tend to align with respect to each other, giving rise to the slight anisotropy of the whole sample. The alignment of the nanoaggregates with respect to each other causes the set of the angles with the shear direction to be ill-spanned compared to an isotropic material. The error bars decrease when the nanoaggregates are ruptured. This happens at quite large shear rates, when the single molecules begin to align in the flow direction, so that the angle of 45 degrees is not clearly visible. Furthermore, at high shear rates, the values of the molecular alignment angle χ_m for different molecule types are ordered according to the molecular weight, the molecules with the highest weight having the lowest alignment angle. It is expected as the difference in velocity from one end of the molecule to the other is larger for large molecules than for small molecules, giving rise to an alignment in the flow direction at lower shear rates.

Finally, Figs. 12 (b) and (c) show the molecular alignment angle of asphaltene and docosane molecules, respectively, at different temperatures. The molecular alignment angle of resin and resinous oil molecules at different temperatures is not displayed for the sake of readability and resembles that of the asphaltene molecules at different temperatures. For both asphaltene and docosane molecules, the lower the temperature, the closer to zero the angle to the flow direction for a given high shear rate. This is consistent with the molecular order parameter being higher for low temperatures than for high temperatures at a given high shear rate. The error bars on the alignment angle of asphaltene molecules are large up to very high shear rates for high temperatures, consistent with the nanoaggregates being maintained up to these high shear rates. Due to the large error bars, the existence of the intermediate range of shear rates identified in Fig. 10 (a) and corresponding to the shear flow disturbing the alignment of the nanoaggregates with respect to each other, does not have a clear effect on the alignment angle of the asphaltene molecules in the flow direction.

C. Intramolecular structure

The intramolecular structure can be characterized by the radius of gyration of each molecule type. The radius of gyration is defined here as $\langle R_g^2 \rangle = \text{trace} \langle \mathbf{R}_g^2 \rangle$, where \mathbf{R}_g^2 is the tensor of gyration given in Eq. (12) and $\langle \cdot \rangle$ is an average over molecules of the same type and over time. Figure 13 shows the variation of the radius of gyration of each molecule type with the shear rate for different temperatures. The variation of the radius of gyration with temperature and with shear rate is very different from one molecule type to another. For asphaltene and resinous oil molecules, Figs. 13 (a) and (c) respectively, the radius of gyration barely changes with the shear rate. It is expected as nearly all carbons in these molecules are aromatic creating a stiff intramolecular structure. However, at the largest shear rates the radius of gyration increases slightly indicating a stretching of the bonds. For both molecule types the radius of gyration increases with increasing temperature, indicating a stretch of the stiff bonds due to a higher velocity of each bead.

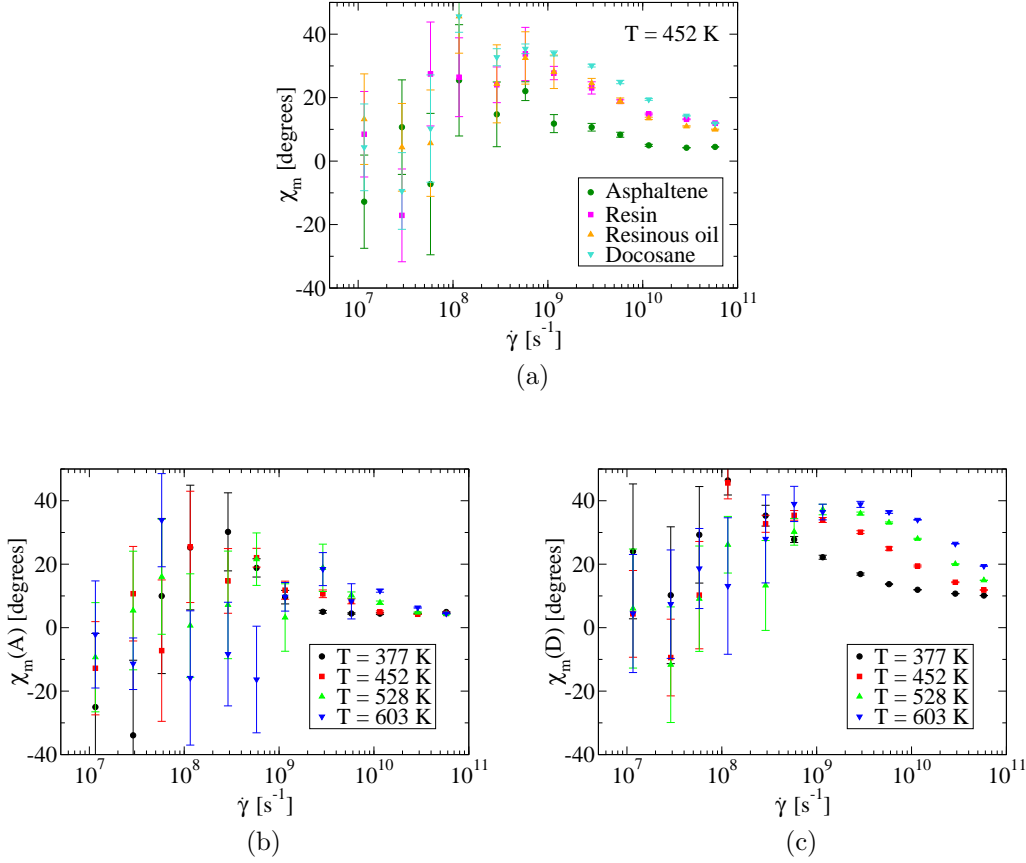


FIG. 12. (Color online) Variation of the molecular alignment angle χ_m with shear rate $\dot{\gamma}$ for three cases: at temperature 452 K and for different molecule types (a), for asphaltene molecules at different temperatures (b), and for docosane molecules at different temperatures (c).

For docosane and resin molecules, Figs. 13 (b) and (d) respectively, the trends are very different. Both molecule types can possess a maximum of their radius of gyration at a given shear rate. For linear molecules such as docosane molecules, this behavior is known [46 and 51] and is attributed to a stretching of the bonds in the flow direction for intermediate shear rates and a coiling up of the whole molecule at very high shear rates when each molecule tumbles more often. The maximum in the radius of gyration of linear molecules is usually associated with a clear minimum of the pressure of the system [46 and 51]. It is not seen in the case of the Cooe bitumen model, probably because other molecules play a part in the value of the pressure as mentioned in Sec. III C. We attribute the maximum seen for resin molecules at

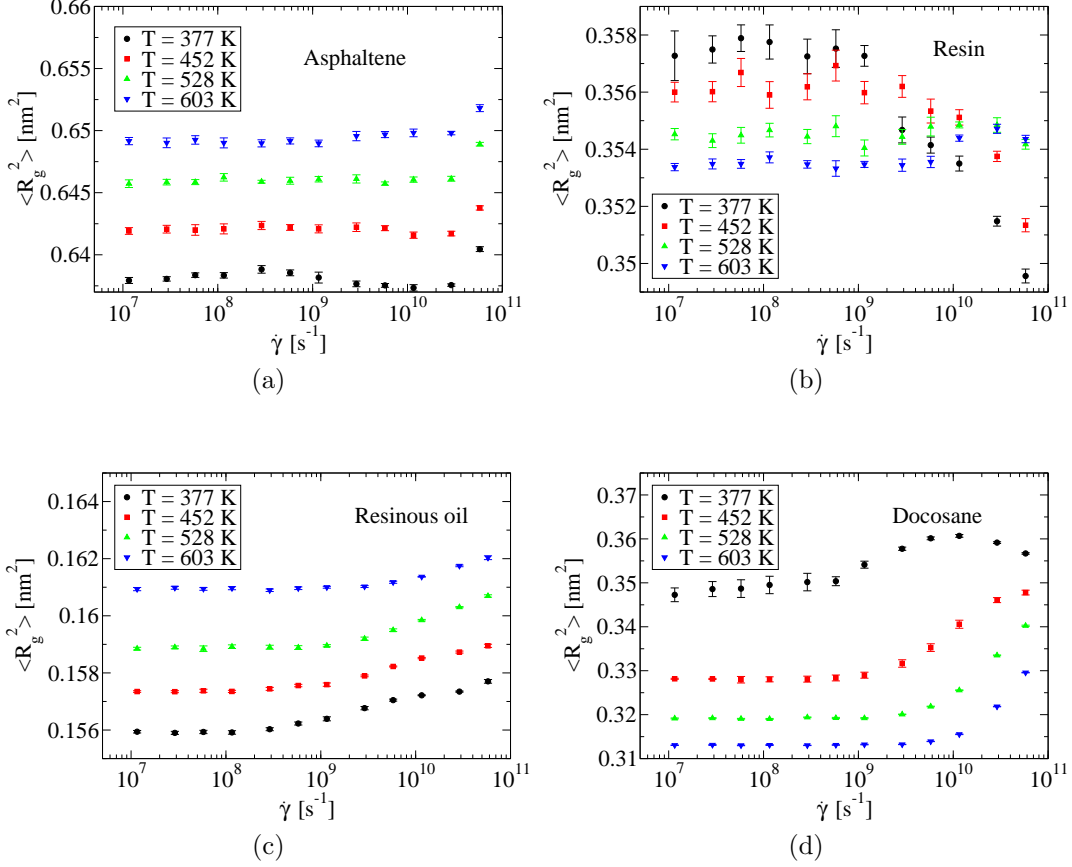


FIG. 13. (Color online) Variation of the radius of gyration with the shear rate for asphaltene (a), resin (b), resinous oil (c) and docosane (d) molecules at different temperatures.

a given shear rate to a similar effect, because resin molecules have some long linear alkyl chains aside from the aromatic plane, in contrast to resinous oil and asphaltene molecules. Finally, for both docosane and resin molecules, the radius of gyration decreases with increasing temperature. This could also be an effect of the larger velocity of each bead, causing coiling of the molecules when the bonds are less stiff than in pure aromatic molecules.

Another informative quantity which can be defined to describe the intramolecular structure is the bond order tensor S_{bond} . It is defined for docosane molecules as:

$$\mathbf{S}_{\text{bond}} = \frac{1}{N_b} \sum_{\alpha=1}^{N_b-1} \left\langle \mathbf{v}_\alpha \otimes \mathbf{v}_\alpha - \frac{1}{3} \mathbf{I} \right\rangle, \quad (15)$$

where N_b is the number of bonds in a docosane molecule, $\langle \cdot \rangle$ is an average over docosane molecules and over time, and \mathbf{v}_α is the unit vector between neighboring

atoms α and $\alpha + 1$ given as:

$$\mathbf{v}_\alpha = \frac{\mathbf{r}_{\alpha+1} - \mathbf{r}_\alpha}{|\mathbf{r}_{\alpha+1} - \mathbf{r}_\alpha|}. \quad (16)$$

In a similar way as for the molecular order tensor \mathbf{S}_m , a bond order parameter S_{bond} and a bond alignment angle χ_{bond} can be defined from the bond order tensor \mathbf{S}_{bond} . These two quantities measure the extent of the alignment of intramolecular bonds to the shear direction and the angle between them. Figures 14 (a) and (b) show the variation of the bond order parameter S_{bond} and the bond alignment angle χ_{bond} of docosane molecules with the shear rate for different temperatures. Both quantities have similar variations with shear rate and temperature as their molecular counterparts. As the shear rate increases, the bonds inside the docosane molecules become more and more aligned in the direction of the shear. This effect gets stronger as the temperature decreases. It is also consistent with the shear-thinning behavior observed in Sec. III A.

The bond order tensor associated with aromatic molecules is less well defined, because the bonds form rings and are not clearly oriented from one end of the molecule to the other. That is why it is not calculated here. However, as shown by the variation of the radius of gyration of the aromatic molecules with the shear rate, the stretching of the molecules is less pronounced for stiff aromatic molecules than for linear ones. Changes in the intramolecular structure of the aromatic molecules probably contribute very little to the shear-thinning behavior generally observed.

V. SUMMARY AND DISCUSSION

Non-equilibrium molecular dynamics simulations under shear have been performed for the first time on a bitumen mixture. They reveal both the non-Newtonian regime of such mixtures and their microscopic structure. The non-Newtonian regime is characterized by a shear rate dependent viscosity, decreasing normal stress coefficients, and a monotonically increasing pressure. The Cooc bitumen is found to be shear-thinning at all temperatures investigated in line with most experimental results on bitumen [6]. The shear-thinning behavior is in agreement with the variation of some characteristics of the inter- and intramolecular structure with the shear

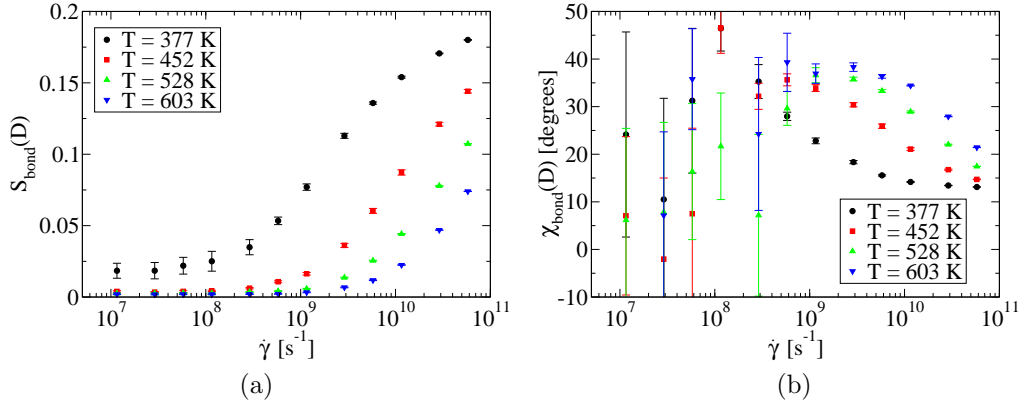


FIG. 14. (Color online) Variation of the bond order parameter S_{bond} (a) and the bond alignment angle χ_{bond} (b) with shear rate $\dot{\gamma}$ for docosane molecules at different temperatures.

rate:

- The saturated hydrocarbon molecules, which can be seen as solvent to the nanoaggregates, align with respect to each other and align their bonds in the shear direction, at all shear rates.
- At high shear rates, the nanoaggregates disintegrate and the single aromatic molecules align in the shear direction.

Some characteristics of the inter- and intramolecular structure of the Cooee bitumen do not change with the shear rate and do not seem to prevent the shear-thinning behavior from being established. They are:

- Until a critical shear rate, dependent on the temperature, the nanoaggregate size distribution is unchanged with increasing shear rate.
- The intramolecular structure of the aromatic molecules, composing the nanoaggregates, is mainly constant up to quite high shear rates.

Finally at high temperatures, there is a domain of intermediate shear rates, where the nanoaggregates still have their equilibrium size, but where the molecular order parameter of asphaltene molecules decreases with increasing shear rate. The decrease of the molecular order parameter indicates a perturbation of the alignment

of the nanoaggregates with respect to each other, due to steric hindrance, by the shear flow. The effect of this local reorganization on the variation of the viscosity with the shear rate is unclear and could be masked by the inter- and intramolecular alignment of the solvent molecules.

In addition, the variation of the rheological properties and of the corresponding molecular structure with temperature was studied. As expected, the viscosity decreases with increasing temperature, following an Arrhenius law. The nanoaggregate size decreases with increasing temperature, which also contributes to the decrease of viscosity with temperature. The increase in viscosity at low temperatures and at a given shear rate explains some of the characteristics of the molecular structure:

- The solvent molecules begin to align in the shear direction at lower shear rates at low temperatures than at high temperatures.
- The nanoaggregates break up at a lower shear rate at low temperatures than at high temperatures. This is also due to the nanoaggregates being longer at low temperatures than at high temperatures.

The study of the structure and rheology of the bitumen mixtures at different temperatures enables us to compare the behavior of a bitumen mixture with other complex systems such as colloidal suspensions, polymer solutions and associative polymer networks. The comparison with these complex systems is relevant because they have similarities with a bitumen mixture. Indeed, the Coocoe bitumen mixture can be seen as a solution of partly flexible nanoaggregates of various sizes [29], with a branched structure [18], in a saturated hydrocarbon solvent, as was already mentioned in Sec. IV A. Furthermore, the nanoaggregate size depends on temperature and shear rate as was seen in Sec. IV.

It is known that both the linear rheological properties such as the zero shear rate viscosity and the non-linear rheological properties of colloidal suspensions and polymer solutions depend on the size, the shape and the polydispersity of the dispersed objects [21, 52, and 53]. In the limit of a dilute solution of such objects, a lot is known on the relation between the intrinsic viscosity $[\eta]$, defined by $\eta_0 = \eta_{0s} + [\eta]\phi + o(\phi)$, where η_{0s} is the zero shear rate viscosity of the solvent and ϕ the volume fraction

of objects, and the shape of the colloids or the topology of the polymers [53]. The shear-thinning behavior at high shear rates can also be related to the topology of the polymers, though for complicated topology such as dendrimers, quantitative models are not available yet to predict the exponent of the decay of the viscosity in the limit of infinite shear rate [21]. At high volume fractions of objects, a higher order expansion of these linear and non-linear rheological properties with the volume fraction is needed, because the interactions between the colloids or polymers cannot be neglected [20]. Bitumen mixtures typically fall in this range, which makes a direct and quantitative comparison with what is known of the rheological properties of dilute and semi-dilute polymer solutions of different topologies difficult.

Another characteristic of bitumen which makes a direct comparison with colloidal suspensions or polymer solutions difficult is the fact that nanoaggregates are maintained by weak interactions and their size depends on temperature and shear rate. This is usually not the case for colloids and for polymer solutions. Theoretical [22, 55–57] and numerical [26, 58–62] studies have been carried out on the linear and non-linear rheological properties of solutions of associative polymers, where the size of the assemblies also depends on temperature and shear rate. There is for example a growing literature on the rheology of telechelic polymer networks [22, 55–57, and 60] and of wormlike micelles [58, 59, 61, and 62]. However, the knowledge in this field is still scarce and very specific to the precise topology of self-assembly studied [26]. It is consequently not so easily transferable to bitumen.

Nevertheless, the current knowledge on the rheology of colloidal suspensions, polymer solutions and associative polymer solutions defines a framework which can be used to better understand bitumen. The size, the polydispersity and the topology of the nanoaggregates as well as the interaction between the nanoaggregates are expected to be the important parameters controlling the rheological properties of bitumen. We hope that the numerical study carried out in this paper can be used as a step towards an analytical modeling of the rheological properties of bitumen based on these parameters.

ACKNOWLEDGEMENTS

This work is sponsored by the grants 1337-00073B and 1335-00762B of the Danish Council for Independent Research | Technology and Production Science. It is in continuation of the Cooee project (CO₂ emission reduction by exploitation of rolling resistance modeling of pavements), sponsored by the Danish Council for Strategic Research. The centre for viscous liquids dynamics "Glass and Time" is supported by the Danish National Research Foundation's grant DNRF61.

Appendix A: Operating splitting algorithm for molecular SLLOD

We have implemented a molecular version of the operator-splitting algorithm described in Ref 32. To our knowledge, it is the first time that this algorithm is adapted to molecular systems. The implementation involves a two-step process: (1) the equations of motion of the molecular centers of mass are solved; (2) the (relatively simple) equations of motion for the particles' positions and velocities relative to the molecular centers of mass are solved and combined with the solutions for centers of mass in order to update the atomic coordinates and velocities. Note that here velocities are the so-called peculiar velocities, i.e. velocities relative to the streaming velocity.

The operator splitting method is an approximation based on a factorization of time propagator U generated by the system's Liouville operator iL . The factorization is denoted $\mathbf{A}\mathbf{B}_1\mathbf{B}_2\mathbf{B}_1\mathbf{A}$ where \mathbf{A} is the operator associated with evolution of the coordinates at fixed momenta, \mathbf{B}_1 is that associated with evolution of the momenta due to the flow only, and \mathbf{B}_2 is that associated with the evolution of momenta in the absence of flow, at fixed particle coordinates. Exact solutions of each set of equations of motion are given by Pan *et al*³². Note that \mathbf{A} and \mathbf{B}_1 appear twice and thus should be integrated over a half time-step each time, although the first instance of \mathbf{A} can be "wrapped" around and put at the end, at the expense of having the positions and velocities and positions a half-step out of sync. The isokinetic thermostat is included in each factor, so that the kinetic energy is exactly conserved (up to round-off error).

For the molecular case the same factorization is made and the above two step procedure is applied for each factor in the approximate propagator. The equations of motion for operator \mathbf{A} are, for our choice of simple shear deformation (where i is a molecular index, α is a particle index within a molecule, and quantities with only the former are center-of-mass quantities):

$$\dot{\mathbf{r}}_{i\alpha} = \frac{\mathbf{p}_{i\alpha}}{m_{i\alpha}} + \dot{\gamma}y_i\hat{x} = \mathbf{v}_{i\alpha} + \dot{\gamma}y_i\hat{x}, \quad (\text{A1})$$

$$\dot{\mathbf{p}}_{i\alpha} = 0 \quad (\text{A2})$$

For later convenience we introduce the atomic and molecular velocities $\mathbf{v}_{i\alpha}$ and \mathbf{v}_i respectively. Focusing on the positions, we multiply by the mass fraction $m_{i\alpha}/M_i$ of the particle α in molecule i and sum over α to get the equation of motion for the center of mass position:

$$\dot{\mathbf{r}}_i = \frac{\mathbf{p}_i}{M_i} + \dot{\gamma}y_i\hat{x} = \mathbf{v}_i + \dot{\gamma}y_i\hat{x}. \quad (\text{A3})$$

This is identical to the position part of the \mathbf{A} operator in Ref. 32 (re-interpreting the index i in their equations as a molecular index), and has the same solution for a time increment Δt (although incorrectly given in that paper; the correct expressions can be found in Ref. 63):

$$x_i(t + \Delta t) = x_i(t) + \Delta t(p_{xi}(t)/M_i + \dot{\gamma}y_i(t)) + (1/2M_i)\Delta t^2\dot{\gamma}p_{yi}(t) \quad (\text{A4})$$

$$y_i(t + \Delta t) = y_i(t) + \Delta t(p_{yi}(t)/M_i) \quad (\text{A5})$$

$$z_i(t + \Delta t) = z_i(t) + \Delta t(p_{zi}(t)/M_i) \quad (\text{A6})$$

Knowing the evolution of the center of mass position during the time step Δt , we can now consider the equations of motion for the relative coordinates of the particles within the molecule by subtracting Eq. (A3) from Eq. (A1), giving

$$\frac{d}{dt}(\mathbf{r}_{i\alpha} - \mathbf{r}_i) = \mathbf{p}_{i\alpha}/m_{i\alpha} - \mathbf{p}_i/M_i = \mathbf{v}_{i\alpha} - \mathbf{v}_i, \quad (\text{A7})$$

where the right side is the particle's velocity relative to the molecule's center of mass and is constant for the \mathbf{A} equations of motion. The solution is therefore (using velocities instead of momenta)

$$\mathbf{r}_{i\alpha}(t + \Delta t) - \mathbf{r}_i(t + \Delta t) = \mathbf{r}_{i\alpha}(t) - \mathbf{r}_i(t) + \Delta t(\mathbf{v}_{i\alpha}(t) - \mathbf{v}_i(t)), \quad (\text{A8})$$

which, upon substituting Eqs. (A4)-A6, gives

$$x_{i\alpha}(t + \Delta t) = x_{i\alpha}(t) + \Delta t(v_{xi\alpha}(t) + \dot{\gamma}y_i(t)) + 1/2\Delta t^2\dot{\gamma}v_{yi}(t) \quad (\text{A9})$$

$$y_{i\alpha}(t + \Delta t) = y_{i\alpha}(t) + \Delta t(v_{yi\alpha}(t)) \quad (\text{A10})$$

$$z_{i\alpha}(t + \Delta t) = z_{i\alpha}(t) + \Delta t(v_{zi\alpha}(t)) \quad (\text{A11})$$

The same procedure is applied to the equations of motion for the \mathbf{B}_1 operator, which for the atomic momenta (at constant positions) are:

$$\frac{d\mathbf{p}_{i\alpha}}{dt} = -\dot{\gamma}\frac{m_{i\alpha}}{M_i}p_{yi}\hat{x} - \alpha_1\frac{m_{i\alpha}}{M_i}\mathbf{p}_i. \quad (\text{A12})$$

Here α_1 is the part of the Gaussian thermostat multiplier ζ associated with conserving the kinetic energy during this part of the integration; it has the expression

$$\alpha_1 = \frac{-\sum_i \dot{\gamma}p_{xi}p_{yi}/M_i}{\sum_i p_i^2/M_i}. \quad (\text{A13})$$

Note that the thermostat term involves only molecular quantities, that is, it is a so-called molecular thermostat which conserves the sum of the translational kinetic energies of the molecules $\sum_i p_i^2/2M_i$. Summing Eq. (A12) over α gives

$$\frac{d\mathbf{p}_i}{dt} = -\dot{\gamma}p_{yi}\hat{x} - \alpha_1\mathbf{p}_i, \quad (\text{A14})$$

which is identical to the \mathbf{B}_1 equation in Ref. 32 (where i was an atomic index). Again the solution must be the same:

$$\mathbf{p}_i(t + \Delta t) = g(\Delta t) (\mathbf{p}_i(t) - \hat{x}\Delta t\dot{\gamma}p_{yi}(t)). \quad (\text{A15})$$

Here $g(\Delta t) = 1/\sqrt{1 - 2c_1\Delta t + c_2\Delta t^2}$ and c_1 and c_2 are expressions involving sums of products of molecular momenta (see Ref. 32). Next we consider the velocity relative to the center of mass. Dividing Eqs. (A12) and A14 by $m_{i\alpha}$ and M_i , respectively, and then subtracting the second from the first gives the equation for the relative velocity:

$$\frac{d}{dt}(\mathbf{v}_{i\alpha} - \mathbf{v}_i) = 0, \quad (\text{A16})$$

i.e. the relative velocity is not affected by the flow or the thermostat—this is of course the point of using molecular SLLOD equations and a molecular thermostat:

they translate each molecules rigidly, without rotation or deformation. The update-expression for an atomic velocity is therefore that which gives the same numerical difference as the update-expression for the center of mass velocity.

$$\mathbf{v}_{i\alpha}(t + \Delta t) = \mathbf{v}_{i\alpha}(t) - \mathbf{v}_i(t) + \mathbf{v}_i(t + \Delta t) \quad (\text{A17})$$

$$= \mathbf{v}_{i\alpha}(t) + (g(\Delta t) - 1)\mathbf{v}_i(t) - g(\Delta t)\Delta t\dot{\gamma}v_{yi}\hat{x}. \quad (\text{A18})$$

For the **B2** equations of motion, the procedure is essentially the same: the velocity of the center of mass obeys the **B₂** equation in Ref. 32 for the atomic case, with solution

$$\mathbf{p}_i(t + \Delta t) = \frac{1 - h}{e - h/e} \left(\mathbf{p}_i(t) + \mathbf{F}_i(t) \frac{1 + h - e - h/e}{(1 - h)\beta} \right) = \mathbf{p}_i(t) + M_i \Delta \mathbf{v}_i \quad (\text{A19})$$

where expressions for $e(\Delta t)$, β and h are given in Ref. 32 (note that the sign of the second term in parentheses was incorrect in Ref. 32, their Eq. (22)). The notation $\Delta \mathbf{v}_i$ for the change in center of mass velocity of molecule i is introduced for use below. The relative velocity obeys:

$$\frac{d}{dt} (\mathbf{v}_{i\alpha} - \mathbf{v}_i) = \mathbf{F}_{i\alpha}/m_{i\alpha} - \mathbf{F}_i/M_i = \mathbf{a}_{i\alpha} - \mathbf{a}_i, \quad (\text{A20})$$

where $\mathbf{a}_{i\alpha}$ and \mathbf{a}_i are the (constant) accelerations. To update the atomic velocities we then have

$$\mathbf{v}_{i\alpha}(t + \Delta t) = \mathbf{v}_{i\alpha}(t) + \Delta v_i + \Delta t(\mathbf{a}_{i\alpha} - \mathbf{a}_i), \quad (\text{A21})$$

where Δv_i is determined from Eq. (A19).

A final technical point: while RUMD uses single precision floating point arithmetic in general, double precision is used for velocities in SLLOD algorithm. In this work, however, to keep the drift of the kinetic energy acceptably low for the small time step and strain rates used, double precision was used for the entire simulation code.

REFERENCES

- ¹J. F. Branthaver, J. C. Pedersen, R. E. Robertson, J. J. Duvall, S. S. Kim, P. M. Harnsberger, T. Mill, E. K. Ensley, F. A. Barbour, and J. F. Schabron, Tech. Rep. SHRP-A-368, Strategic Highway Research Program (1993).
- ²D. A. Anderson, D. W. Christensen, H. U. Bahia, R. Dongre, M. G. Sharma, C. E. Antle, and J. Button, Tech. Rep. SHRP-A-369, Strategic Highway Research Program (1994).
- ³J. C. Petersen, Transportation Research Circular E-C140, Transportation Research Board (2009).
- ⁴S. E. Johnson, W. Y. Svrcek, and A. K. Mehrotra, *Ind. Eng. Chem. Res.* **26**, 2290 (1987).
- ⁵L.-I. Palade, P. Attané, and S. Camaro, *Rheol. Acta* **39**, 180 (2000).
- ⁶D. Sybilski, *Mater. Struct.* **26**, 15 (1993).
- ⁷O. Ukwuoma and B. Ademodi, *Fuel Processing Technology* **60**, 95 (1999).
- ⁸M. García-Morales, P. Partal, F. J. Navarro, F. Martínez-Boza, C. Gallegos, N. González, O. González, and M. E. Muñoz, *Fuel* **83**, 31 (2004).
- ⁹P. Michalica, I. B. Kazatchkov, J. Stastna, and L. Zanzotto, *Fuel* **87**, 3247 (2008).
- ¹⁰J. M. Dealy and J. Wang, *Melt Rheology and its Applications in the Plastics Industry* (Springer, New York, 2013).
- ¹¹O. C. Mullins, *Annu. Rev. Anal. Chem.* **4**, 393 (2011).
- ¹²J. Murgich, J. Rodríguez M., and Y. Aray, *Energy & Fuels* **10**, 68 (1996).
- ¹³J. H. Pacheco-Sánchez, I. P. Zaragoza, and J. M. Martínez-Magadán, *Energy & Fuels* **17**, 1346 (2003).
- ¹⁴F. Frigerio and D. Molinari, *Comp. Theor. Chem.* **975**, 76 (2011).
- ¹⁵P. Ungerer, D. Rigby, B. Leblanc, and M. Yiannourakou, *Mol. Simulat.* **40**, 115 (2014).
- ¹⁶L. Zhang and M. L. Greenfield, *J. Chem. Phys.* **127**, 194502 (2007).
- ¹⁷J. S Hansen, C. A. Lemarchand, E. Nielsen, J. C. Dyre, and T. Schrøder, *J. Chem. Phys.* **138**, 094508 (2013).
- ¹⁸C. A. Lemarchand, T. B. Schrøder, J. C. Dyre, and J. S. Hansen, *J. Chem. Phys.* **139**, 124506 (2013).

- ¹⁹D. D. Li and M. L. Greenfield, *Fuel* **115**, 347 (2014).
- ²⁰P. Coussot and C. Ancey, *Phys. Rev. E* **59**, 4445 (1999).
- ²¹R. G. Winkler, D. A. Fedosov, and G. Gompper, *Curr. Opin. Colloid Interface Sci.* **19**, 594 (2014).
- ²²A. Vaccaro and G. Marrucci, *J. Non-Newtonian Fluid Mech.* **92**, 261 (2000).
- ²³D. J. Evans and G. P. Morriss, *Statistical Mechanics of Nonequilibrium Liquids* (Academic, London, 1990).
- ²⁴B. D. Todd and P. J. Daivis, *Molecular Simulation* **33**, 189 (2007).
- ²⁵T. C. Le, B. D. Todd, P. J. Daivis, and A. Uhlherr, *J. Chem. Phys.* **131**, 044902 (2009).
- ²⁶Z. Li, H. Djohari, and E. E. Dormidontova, *J. Chem. Phys.* **133**, 184904 (2010).
- ²⁷N.-T. Van-Oanh, C. Houriez, and B. Rousseau, *Phys. Chem. Chem. Phys.* **12**, 930 (2009).
- ²⁸CO2 emission reduction by exploitation of rolling resistance modelling of pavements, <http://www.cooee-co2.dk/>.
- ²⁹C. A. Lemarchand, T. B. Schröder, J. C. Dyre, and J. S. Hansen, *J. Chem. Phys.* **141**, 144308 (2014).
- ³⁰A. Wiehe and K.S. Liang, *Fluid Phase Equil.* **117**, 201 (1996).
- ³¹ASTM. 1995, *Annual Book of Standards* (American Society for Testing and Materials, Philadelphia, 1995); method D-2007.
- ³²G. Pan, J. F. Ely, C. McCabe, and D. J. Isbister, *J. Chem. Phys.* **122**, 094114 (2005).
- ³³N. Bailey, L. Bøhling, J. S. Hansen, T. Ingebrigsten, H. Larsen, C. A. Lemarchand, U. R. Pedersen, T. Schröder, and A. A. Veldhorst, <http://rumd.org>.
- ³⁴J. H. Irving and J. G. Kirkwood, *J. Chem. Phys.* **18**, 817 (1950).
- ³⁵R. B. Bird, C. F. Curtiss, R. C. Armstrong, and O. Hassager, *Dynamics of Polymeric Liquids* (Wiley, New York, 1987).
- ³⁶P. J. Farrington, C. J. Hawker, J. M. Frechet, and M. E. MacKay, *Macromolecules* **31**, 5043 (1998).
- ³⁷C.-Y. Liu, J. He, R. Keunings, and C. Bailly, *Macromolecules* **39**, 8867 (2006).
- ³⁸X. Lu and U. Isacsson, *Constr. Build. Mater.* **14**, 79 (2000).

- ³⁹J. G. Guan, M. Kariznovi, H. Nourozieh, and J. Abedi, *J. Chem. Eng. Data* **58**, 611 (2013).
- ⁴⁰P. Partal, F. Martínez-Boza, B. Conde, and C. Gallegos, *Fuel* **78**, 1 (1999).
- ⁴¹M. Masoori and M. L. Greenfield, *J. Chem. Phys.* **141**, 124504 (2014).
- ⁴²S. Bair, C. McCabe, and P. T. Cummings, *Phys. Rev. Lett.* **88**, 058302 (2002).
- ⁴³M. Van Gorp and J. Palmen, *Rheol. Bull.* **67**, 5 (1998).
- ⁴⁴J. Ge, B. D. Todd, G. Wu, and R. J. Sadus, *Phys. Rev E* **67**, 061201 (2003).
- ⁴⁵L. Separdar, N. P. Bailey, T. B. Schrøder, S. Davatolhagh, and J. C. Dyre, *J. Chem. Phys.* **138**, 154505 (2013).
- ⁴⁶J. T. Bosko, B. D. Todd, and R. J. Sadus, *J. Chem. Phys.* **121**, 12050 (2004).
- ⁴⁷M. Doi and S. F. Edwards, *The theory of polymer dynamics* (Clarendon, Oxford, 1986).
- ⁴⁸S. Förster, M. Konrad, and P. Lindner, *Phys. Rev. Lett.* **94**, 017803 (2005).
- ⁴⁹B. Aguilera-Mercado, C. Herdes, J. Murgich, and E. A. Müller, *Energy & Fuels* **20**, 327 (2006).
- ⁵⁰J. L. S. Wales, *The Application of Flow Birefringence to Rheological Studies of Polymer Melts* (Delft University Press, Delft, 1976).
- ⁵¹R. Khare, J. de Pablo, and A. Yethiraj, *J. Chem. Phys.* **107**, 6956 (1997).
- ⁵²D. B. Genovese, *Adv. Colloid Interface Sci.* **171-172**, 1 (2012).
- ⁵³M. L. Mansfield and J. F. Douglas, *J. Chem. Phys.* **139**, 044901 (2013).
- ⁵⁴J. T. Bosko, B. D. Todd, and R. J. Sadus, *J. Chem. Phys.* **123**, 034905 (2005).
- ⁵⁵T. Indei, T. Koga, and F. Tanaka, *Macromol. Rapid Commun.* **26**, 701 (2005).
- ⁵⁶A. Tripathi, K. C. Tam, and G. H. McKinley, *Macromolecules* **39**, 1981 (2006).
- ⁵⁷T. Koga and F. Tanaka, *Macromolecules* **43**, 3052 (2010).
- ⁵⁸M. Kröger and R. Makhoulfi, *Phys. Rev. E* **53**, 2531 (1996).
- ⁵⁹A. Milchev, J. Wittmer, and D. Landau, *Eur. Phys. J. B* **12**, 241 (1999).
- ⁶⁰D. Bedrov, G. D. Smith, and J. F. Douglas, *Europhys. Lett.* **59**, 384 (2002).
- ⁶¹J. Padding, E. Boek, and W. Briels, *J. Chem. Phys.* **129**, 074903 (2008).
- ⁶²C. C. Huang, H. Xu, and J. Ryckaert, *Europhys. Lett.* **131**, 58002 (2008).
- ⁶³F. Zhang, D. J. Searles, D. J. Evans, J. S. den Toom Hansen, and D. J. Isbister, *J. Chem. Phys.* **111**, 18 (1999).